



## Impact of a monotonic advection scheme with low numerical diffusion on transport modeling of emissions from biomass burning

S. R. Freitas<sup>1</sup>, L. F. Rodrigues<sup>1</sup>, K. M. Longo<sup>2</sup> and J. Panetta<sup>1</sup>

<sup>1</sup> Center for Weather Forecasting and Climate Studies, INPE, Cachoeira Paulista, Brazil.

<sup>2</sup> Earth System Science Center, INPE, São José dos Campos, Brazil.

An advection scheme, which maintains the initial monotonic characteristics of a tracer field being transported and at the same time produces low numerical diffusion, is implemented in the Coupled Chemistry-Aerosol-Tracer Transport model to the Brazilian developments on the Regional Atmospheric Modeling System (CCATT-BRAMS). Several comparisons of transport modeling using the new and original (non-monotonic) CCATT-BRAMS formulations are performed. Idealized 2-D non-divergent or divergent and stationary or time-dependent wind fields are used to transport sharply localized tracer distributions, as well as to verify if an existent correlation of the mass mixing ratios of two interrelated tracers is kept during the transport simulation. Further comparisons are performed using realistic 3-D wind fields. We then perform full simulations of real cases using data assimilation and complete atmospheric physics. In these simulations, we address the impacts of both advection schemes on the transport of biomass burning emissions and the formation of secondary species from non-linear chemical reactions of precursors. The results show that the new scheme produces much more realistic transport patterns, without generating spurious oscillations and under- and overshoots or spreading mass away from the local peaks. Increasing the numerical diffusion in the original scheme in order to remove the spurious oscillations and maintain the monotonicity of the transported field causes excessive smoothing in the tracer distribution, reducing the local gradients and maximum values and unrealistically spreading mass away from the local peaks. As a result, huge differences (hundreds of %) for relatively inert tracers (like carbon monoxide) are found in the smoke plume cores. In terms of the secondary chemical species formed by non-linear reactions (like ozone), we found differences of up to 50% in our simulations.

DOI:10.1029/2011MS000084

### 1. Introduction

The advection equation is a fundamental part of any fluid dynamics model. In the context of atmospheric constituents, this equation describes the transport of scalar properties (e.g., mass density and mass mixing ratio) by the wind flow. As stated by Rood [1987], the advent of atmospheric chemistry transport models to study the environmental impacts caused by manmade greenhouse gases, aerosol particles and other pollutants requires the use of accurate numerical advection schemes, primarily to precisely simulate the transport of plumes produced by sharply localized sources. On the other hand, as explicit simulation of clouds by so-called cloud resolving/permitting models becomes frequent, the use of more accurate advection schemes is also increasing, since clouds present sharp boundaries. One

important reason for the need for more accurate methods is the difficulty of most advection schemes in properly transporting structures that have strong gradients without generating spurious oscillations, overshooting and even negative values of positive-definite fields, like mass mixing ratios.

Several authors have reported on the importance of using more accurate advection schemes to improve several aspects of atmospheric numerical simulations. Skamarock and Weisman [2009] demonstrated the impact of a positive-definite transport scheme for moisture in numerical

#### To whom correspondence should be addressed.

S. R. Freitas, Center for Weather Forecasting and Climate Studies, INPE, Rodovia Presidente Dutra, km 39, Cachoeira Paulista, 12630-000, Brazil. (saulo.freitas@cptec.inpe.br)

weather forecasting. The new scheme significantly reduced the large positive bias in surface precipitation forecasts found when the non-positive-definite advection scheme was used by the model. Wang *et al.* [2009] evaluated the performance of advection scheme formulations in the Advanced Research Weather Research and Forecasting Model (WRF-ARW). This modeling system was used to produce large-eddy simulations focusing on aerosol-cloud interactions studies. The authors tested the original formulation based on the Runge–Kutta time-integration scheme, with the option of using a positive-definite (PD) flux limiter. The PD option eliminated the negative scalar mixing ratios generated by the basic formulation, but maintained spurious oscillations with overshoots of up to 20%. They then implemented a new option using a monotonic flux limiter (MNT) that minimized the dispersion errors with a small augmentation of the numerical diffusion. The simulations using the PD and the MNT options showed considerable differences in the cloud droplet and albedo fields.

When developing advection schemes, the following properties are frequently desired [e.g., Rood, 1987; Lauritzen *et al.*, 2011]: (1) mass conserving, (2) monotonic, positive-definite and non-oscillatory, (3) low numerical diffusion, (4) local, (5) accurate, (6) stable, (7) efficient from a computational point of view, (8) multi-tracer computational efficiency (reuse of repeated calculations), (9) retains tracer non-linear correlations and (10) multi-component mass conserving. However, most advection schemes are not able to simultaneously accomplish all the properties listed above.

This paper describes and evaluates the new advection scheme implemented in the CCATT-BRAMS regional atmospheric chemistry transport model [Freitas *et al.*, 2005, 2009; Longo *et al.*, 2010, also The Chemistry-CATT BRAMS model: A new efficient tool for atmospheric chemistry studies at local and regional scales, submitted to *Geoscientific Model Development*, 2011). BRAMS is derived from the Regional Atmospheric Modeling System (RAMS) [Walko *et al.*, 2000] with several implementations (see Freitas *et al.* [2009] for details) to improve atmospheric simulations over tropical and sub-tropical areas of South America. CCATT-BRAMS is used in this study to simulate the emission, transport and chemical transformation of trace gases produced by biomass burning over South America.

This paper is organized as follows. Section 2 briefly introduces the linear advection equation and the two numerical schemes used in this study. In Section 3, idealized wind flows and tracer distributions are employed to quantitatively evaluate both advection schemes. This section ends with two evaluations using real wind flows. Section 4 performs evaluations and discusses results for a real case associated with a biomass burning plume. The summary and conclusions are presented in Section 5.

## 2. The Advection Schemes

The 3-D linear advection equation for a scalar quantity reads

$$\frac{\partial \eta}{\partial t} + \vec{v} \cdot \nabla \eta = 0, \quad (1)$$

where  $\vec{v} = (u, v, w)^T$  is the wind field and  $\eta = \frac{\rho}{\rho_a}$  is the mass mixing ratio of the tracer being advected. Here  $\rho$  and  $\rho_a$  are the tracer density and dry air density, respectively. Equation (1) is also referred to as the advective form of the advection equation. The dry air density obeys the mass continuity equation

$$\frac{\partial \rho_a}{\partial t} + \nabla \cdot (\rho_a \vec{v}) = 0. \quad (2)$$

Combining equations (1) and (2), the flux form of the advection equation can be derived

$$\frac{\partial}{\partial t} (\rho_a \eta) + \nabla \cdot (\rho_a \eta \vec{v}) = 0. \quad (3)$$

One important property of the advection equation is that equation (1) is equivalent to

$$\frac{d\eta}{dt} = 0, \quad (4)$$

or  $\eta$  constant from the Lagrangian point of view (following the air parcel). This also means that the advection itself cannot create a new maximum or minimum of the tracer mixing ratio field being advected. So, the following condition holds for  $\eta$  at any time  $t > 0$

$$\eta(t) \in [\min(\eta(t=0)), \max(\eta(t=0))]$$

where min and max mean the global minimum and maximum values. However, for the density field the condition above is only obeyed when the wind field is non-divergent. One critical point of any advection scheme, when transporting sharply localized tracer fields, is the generation of oscillations around the strong gradients (known as Gibbs phenomenon [Hundsdoerfer and Verwer, 2007]). Monotonic schemes are used to prevent or attenuate the Gibbs phenomenon. Formally, monotonic numerical schemes are ones which, given an initial distribution which is monotonic before advection, produce a monotonic distribution after advection. Consequently, they neither create new extrema in the solution nor amplify existing extrema. Non-monotonic schemes can generate negative mass concentrations (due to undershoots), which does not make physical sense, but also give unstable chemical reactions, from a numerical point of view. Also, the amplification of the actual maximum values (overshoots) of concentrations of reactive species can have huge impacts, mainly if the reaction is non-linear.

Another important property of the advection equation is that an initially homogeneous mixing ratio ( $\eta(x, y, z, t=0)$  constant  $\forall(x, y, z)$ , where  $x$ ,  $y$  and  $z$  are the three

spatial coordinates) under advection by any type of wind field will remain exactly the same as the initial situation. This property is called the preservation of constancy and it is a primary requirement for any numerical advection scheme.

One current approach to solving the 3-D advection equation makes use of the splitting operator technique [Yanenko, 1971; McRae et al., 1982; Lanser and Verwer, 1998]. In this methodology, the 3-D problem (e.g., equation (1)) is split into three 1-D problems in the following way

$$\begin{cases} \left(\frac{\partial \eta}{\partial t}\right)_x = -u \frac{\partial \eta}{\partial x} \\ \left(\frac{\partial \eta}{\partial t}\right)_y = -v \frac{\partial \eta}{\partial y} \\ \left(\frac{\partial \eta}{\partial t}\right)_z = -w \frac{\partial \eta}{\partial z} \end{cases} \quad (5)$$

Each direction is solved independently and then the various changes resulting from the separate partial calculations are combined to provide the global solution. The global solution can be achieved by parallel or sequential (unidirectional or symmetric) techniques. In the sequential technique (used in this work), each partial problem is solved using the solution just updated from the application of the previous partial operator as the initial condition. For example, Crowley [1968] solves the 2-D advection equation by performing two consecutive passes

$$\eta^* = \mathbf{ADV}_X[\eta(t)] \Rightarrow \eta(t + \Delta t) = \mathbf{ADV}_Y[\eta^*]$$

where the symbol  $\mathbf{ADV}$  stands for the one-dimensional (or partial) advection operator.

In the parallel technique, each partial problem solution uses the same initial condition and then the global solution is obtained from a simple sum of the partial solutions. In this case for a 2-D problem, partial increments due to each one-dimensional advection are determined as described below

$$\begin{cases} \Delta \eta_X(t + \Delta t) = \mathbf{ADV}_X[\eta(t)] - \eta(t) \\ \Delta \eta_Y(t + \Delta t) = \mathbf{ADV}_Y[\eta(t)] - \eta(t), \end{cases}$$

then, the global solution at time  $t + \Delta t$  is given by

$$\eta(t + \Delta t) = \Delta \eta_X(t + \Delta t) + \Delta \eta_Y(t + \Delta t) + \eta(t).$$

The rest of this section summarizes the methods used to solve the 1-D advection equation within the CCATT-BRAMS modeling system.

### 2.1. The Tremback et al. Formulation

In the original formulation, the advection scheme in CCATT-BRAMS is described by Tremback et al. [1987].

First of all, the advective scheme is configured in flux form in order to conserve mass. Considering the x-direction, the right side of equation (5) can be generically written as:

$$\begin{aligned} \left(-u \frac{\partial \eta}{\partial x}\right)_i &= -\frac{1}{\rho_a} \frac{\partial}{\partial x} (\rho_a \eta u) + \eta \frac{\partial}{\partial x} (\rho_a u) \approx -\frac{1}{\rho_a \Delta x_i} \\ &\left\{ \left( (\rho_a F)_{i+1/2} - (\rho_a F)_{i-1/2} \right) - \eta_j \left( (\rho_a u)_{i+1/2} - (\rho_a u)_{i-1/2} \right) \right\}, \end{aligned} \quad (6)$$

where  $u$  is the wind component in the  $x$  direction,  $\rho_a$  is the dry air density, and  $\eta$  is the mass mixing ratio of the tracer being advected. The subscript  $i$  references a particular grid point. The subscript  $i+1/2$  ( $i-1/2$ ) means that the quantity is evaluated at the right (left) face of the grid point  $i$ . The numerical solution for the advection fluxes is forward upstream of second-order given by [Crowley, 1968]:

$$F_{i+1/2} = \frac{\Delta x_i}{\Delta t} \left[ \frac{\alpha_i}{2} (\eta_i + \eta_{i+1}) + \frac{\alpha_i^2}{2} (\eta_i - \eta_{i+1}) \right], \quad (7)$$

where  $\alpha = u\Delta t/\Delta x$  is the Courant–Friedrichs–Lewy (CFL) number, with  $\Delta t$  and  $\Delta x$  the model time step and grid spacing, respectively. In the current implementation, the fluxes are reduced to first order ( $F_{i+1/2} = \frac{\Delta x_i}{\Delta t} \alpha_i \eta_i$ ), if necessary, to retain positive-definiteness of scalar quantities. According to the code documentation, the quantity will remain positive definite provided that both fluxes are exiting the box and  $|\alpha_i| + |\alpha_{i+1}| < 1$ . However, the former procedure does not always guarantee non-negative mixing ratio values and thus further clipping is necessary, mainly when tracer distributions which show strong gradients are advected. Here, the clipping procedure means that negative mass mixing ratio values are converted to zero. In addition, there is no mass compensation for the grid boxes with positive mass mixing ratios, so conservation of total mass is not exactly obeyed.

The scheme requires only information from the nearest neighbors of each model grid box, simplifying parallel computational implementation. This also reduces the amount of data to be exchanged among the computer nodes when using Message Passing Interface (MPI). The full 3-D solution for the advection equation is obtained using unidirectional sequential splitting, following the order  $x \rightarrow y \rightarrow z$ .

### 2.2. The Walcek Formulation

The new formulation implemented for the advection scheme in CCATT-BRAMS was developed by Walcek [2000, hereinafter W2000]. W2000 solves the equation

$$\frac{\partial}{\partial t} (\rho_a \eta) + \frac{\partial}{\partial x} (\rho_a \eta u) = 0, \quad (8)$$

evaluating the first guess for the mass mixing ratio at time  $t + \Delta t$  using the following equation

$$\eta_i^{guess} = \frac{1}{D_d} \left[ \eta_i^t D_{d-1} - \frac{(\Delta t \rho_a \eta_f u)_{i+1/2}}{\Delta x_i} + \frac{(\Delta t \rho_a \eta_f u)_{i-1/2}}{\Delta x_i} \right]. \quad (9)$$

Here, following the description given by W2000,  $\eta_f$  is the average mixing ratio within the fluid flowing across each cell edge during time step  $\Delta t$ , and  $D_{d-1}$  and  $D_d$  are the dimensionally dependent fluid air densities at the beginning and end of the time step. Also, the fluxes  $(\Delta t \rho_a \eta_f u)_{i\pm 1/2}$  are evaluated assuming a linear distribution of the tracer within each grid cell, following *Van Leer's* [1977] approach. The following steps are taken to impose monotonicity of the solution:

1.  $(\eta_f)_{i\pm 1/2}$  is constrained to fall in the range of the mixing ratios on either side of the interface where the fluxes are evaluated

$$\begin{cases} \min(\eta_i, \eta_{i+1}) < (\eta_f)_{i+1/2} < \max(\eta_i, \eta_{i+1}), & u_{i+1/2} \geq 0 \\ \min(\eta_i, \eta_{i-1}) < (\eta_f)_{i-1/2} < \max(\eta_i, \eta_{i-1}), & u_{i-1/2} < 0. \end{cases} \quad (10)$$

2. Outflowing fluxes are adjusted so that the updated mixing ratios never exceed or fall below the physically constrained highest ( $\eta_{\max}^{t+\Delta t}$ ) and lowest ( $\eta_{\min}^{t+\Delta t}$ ) allowed mixing ratios:

- (1) The upper and lower limits are given by

$$\begin{cases} \eta_{\min}^{t+\Delta t} = \min(\eta_i, \eta_{i-1}), \quad \eta_{\max}^{t+\Delta t} = \max(\eta_i, \eta_{i-1}), & u_{i-1/2} \geq 0 \\ \eta_{\min}^{t+\Delta t} = \min(\eta_i, \eta_{i+1}), \quad \eta_{\max}^{t+\Delta t} = \max(\eta_i, \eta_{i+1}), & u_{i-1/2} < 0, \end{cases} \quad (11)$$

- (2) If  $\eta_i^{guess}$  violates these monotonic constraints, the updated mixing ratio is set to the violated limit

$$\eta_i^{t+\Delta t} = \max[\min(\eta_{\max}^{t+\Delta t}, \eta_i^{guess}), \eta_{\min}^{t+\Delta t}]. \quad (12)$$

- (3) Then the outflowing flux is adjusted so that  $\eta_i^{t+\Delta t}$  becomes the violated limit

$$\begin{cases} (\Delta t \rho_a \eta_f u)_{i+1/2} = [\eta_i^t D_{d-1} - \eta_i^{t+\Delta t} D_d] \Delta x_i + \\ \quad (\Delta t \rho_a \eta_f u)_{i-1/2}, & u_{i+1/2} \geq 0 \\ (\Delta t \rho_a \eta_f u)_{i-1/2} = [\eta_i^{t+\Delta t} D_d - \eta_i^t D_{d-1}] \Delta x_i + \\ \quad (\Delta t \rho_a \eta_f u)_{i+1/2}, & u_{i-1/2} < 0. \end{cases} \quad (13)$$

The numerical diffusion, which erroneously spreads mass away from local peaks, is reduced by introducing a numerical parameter. This parameter adjusts fluxes at two cell edges around local extremes, reducing the numerical diffusion.

### 3. Numerical Experiments

In this section, several numerical experiments are performed to evaluate both advection schemes. We start with idealized wind flows and then we perform real experiments using atmospheric analysis data to provide initial and boundary conditions for the model integration. To evaluate the numerical results when the true solution is known exactly, the following normalized standard errors are used [Williamson et al., 1992], assuming we use a limited-area domain in Cartesian coordinates and all grid boxes have identical sizes (which is the case for Sect. 3.1):

$$l_1 = \frac{\sum_{ij} |\phi - \phi_T|}{\sum_{ij} |\phi_T|}, \quad (14)$$

$$l_2 = \left[ \frac{\sum_{ij} (\phi - \phi_T)^2}{\sum_{ij} (\phi_T)^2} \right]^{1/2}, \quad (15)$$

$$l_\infty = \frac{\max_{ij} |\phi - \phi_T|}{\max_{ij} |\phi_T|}, \quad (16)$$

where  $\phi$  and  $\phi_T$  are the numerical and true solution, respectively, of the quantity being advected. Here, the sum and max operators extend over the entire model domain. The best score is the closest to zero. We also evaluate the mass conservation capability of each advection scheme by defining the following parameter

$$m_{err} = \frac{m_f - m_i}{m_i}. \quad (17)$$

Here, the quantities  $m_f$  and  $m_i$  are the final and initial total mass of the tracer being advected. Table 1 introduces the nomenclature we will follow hereafter to refer to the advection scheme used in the numerical experiments.

**Table 1.** Nomenclature of the Advection Schemes Used in this Work

Nomenclature	Advection Scheme Used
orig	Tremback et al. [1987]
mnt	Walcek [2000]

### 3.1. Idealized Wind Flows and Tracer Distributions

#### 3.1.1. Solid Body Rotation Under a Non-divergent Rotational 2-D Wind Field

This is a traditional wind field used by several authors to test their advection schemes [e.g., Prather, 1986; Lin and Rood, 1996; W2000]. It is easy to implement, and with this wind field, after a complete rotation, the solution of the tracer mixing ratio field will be exactly the same as the initial field. The 2-D wind field  $\vec{v} = (u, v)^T$  is stationary (time independent) and given by

$$\begin{cases} u(x, y) = -\frac{U_0}{a}(y - y_0) \\ v(x, y) = +\frac{U_0}{b}(x - x_0), \end{cases} \quad (18)$$

where  $U_0$  is the amplitude of the each wind component, in this case  $\pi$  m/s, and  $x_0 = 50$  m and  $y_0 = 50$  m are the center of model grid domain. The constants  $a$  and  $b$  are the lengths of the model domain which are defined below. The boundary condition is determined by the flow direction. For the inflow condition, the background mass mixing ratio is transported towards the interior of the model domain. In case of outflow, the tracer flows out of the domain. It is easy to show that  $\nabla \cdot (u, v)^T = 0$ . The integration of the advection equation is performed on a horizontal grid spacing of 1 meter at each direction with the model domain composed by  $100 \times 100$  grid boxes. To test the CFL restriction, four experiments are done using different time steps (see Table 2). The initial tracer field has the form of a square of length 20 grid boxes filled with  $2.5 \cdot 10^{-3}$  arbitrary units (hereafter au) in the region  $30 \text{ m} \leq x < 50 \text{ m}$  and  $30 \text{ m} \leq y < 50 \text{ m}$ , as shown in Figure 1a. Note that the advection is performed on a tracer background equal to zero and the total mass of the tracer is numerically equal to 1. The air density at the initial time is  $1 \text{ kg/m}^3$  and, as the wind field is non-divergent, it will remain exactly the same during the integration. Figures 1c and 1d show the numerical solution for the tracer mixing ratio after a full rotation using the orig and the mnt advection schemes, respectively, for a time step of 0.1 s, which correspond to a CFL number of  $\pi/10$ . While the orig solution hardly resembles the exact solution (Figure 1a), the mnt solution provides much better agreement. Both schemes do not create negative mixing ratios; however, the

orig one generates spurious new maxima as seen in Figure 1b. The same figure shows perfect agreement between the exact and mnt solutions in most grid boxes, only showing discrepancies in the location of sharp gradients due to the low numerical diffusion introduced by the scheme.

The corresponding evaluation using the criteria introduced in Sect. 3 is presented in Table 2. Besides the experiment shown in Figure 1, three additional runs were performed using time steps of 1/4, 1/3 and 1/2 s, which correspond to CFL numbers of  $\pi/4$ ,  $\pi/3$  and  $\pi/2$ , respectively. Note that, for single precision, the machine precision is about  $10^{-7}$  for the mass absolute error and about  $10^{-5}\%$  for the relative one. From Table 2, the mnt scheme preserves the total mass better than the orig scheme, and its relative error ( $m_{err}$ ) is in the range of the machine precision. In addition, the mnt scheme shows much better scores for the normalized standard errors.

#### 3.1.2. Deformational Non-divergent and Time-Dependent 2-D Wind Flow

Nair and Lauritzen [2010, hereinafter NL2010] provide several recommendations for testing advection schemes. One is using a periodic time-dependent and non-divergent 2-D wind field given by:

$$\begin{cases} u(x, y, t) = U_0 \sin^2(a\pi x) \sin(2a\pi y) \cos(\pi t/T) \\ v(x, y, t) = -U_0 \sin^2(a\pi y) \sin(2a\pi x) \cos(\pi t/T), \end{cases} \quad (19)$$

where  $U_0$  is the amplitude of each wind component, in this case 80 m/s,  $a$  is a constant given by  $\pi/1000 \text{ km}^{-1}$  and  $T = 6 \text{ h}$  is the time period. The time integration is performed in the interval  $0 \leq t \leq T$ . Following NL2010, the term  $\cos(\pi t/T)$  was recommended by LeVeque [1996] to impose a reverse flow field  $(u, v)$  after time  $t = T/2$  and then bring the tracer field back to its initial shape and position at time  $t = T$ , providing the exact solution to evaluate the numerical one. Again, it can be shown that  $\nabla \cdot (u, v)^T = 0$  at any time  $t$ . In this test, the integration of the advection equation is performed with 10 km grid spacing in each direction with the model domain composed of  $100 \times 100$  grid boxes. Here we set a time step of 100 s, which corresponds to the maximum CFL number of 0.8. To test both advection schemes under this wind flow, four initial tracer

**Table 2.** The Normalized Standard and Mass Conservation Errors for the Rotational Non-divergent Flow Test Using Four CFL Numbers<sup>a</sup>

CFL Number and the Total Number of Time Steps	$l_1$ orig	$l_1$ mnt	$l_2$ orig	$l_2$ mnt	$l_\infty$ orig	$l_\infty$ mnt	$m_{err}$ (%) orig	$m_{err}$ (%) mnt
$\pi/10 - 1000$	0.471	0.132	0.443	0.270	0.857	0.937	$-1 \cdot 10^{-4}$	$-6 \cdot 10^{-5}$
$\pi/4 - 400$	0.449	0.116	0.420	0.240	0.842	0.827	$-2 \cdot 10^{-4}$	$-7 \cdot 10^{-5}$
$\pi/3 - 300$	0.456	0.111	0.408	0.220	0.861	0.757	$-2 \cdot 10^{-4}$	$-6 \cdot 10^{-5}$
$\pi/2 - 200$	U	0.103	U	0.193	U	0.686	U	$-1 \cdot 10^{-4}$

<sup>a</sup>The total number of time steps is the amount needed for a full revolution. The letter 'U' means that model integration became unstable.

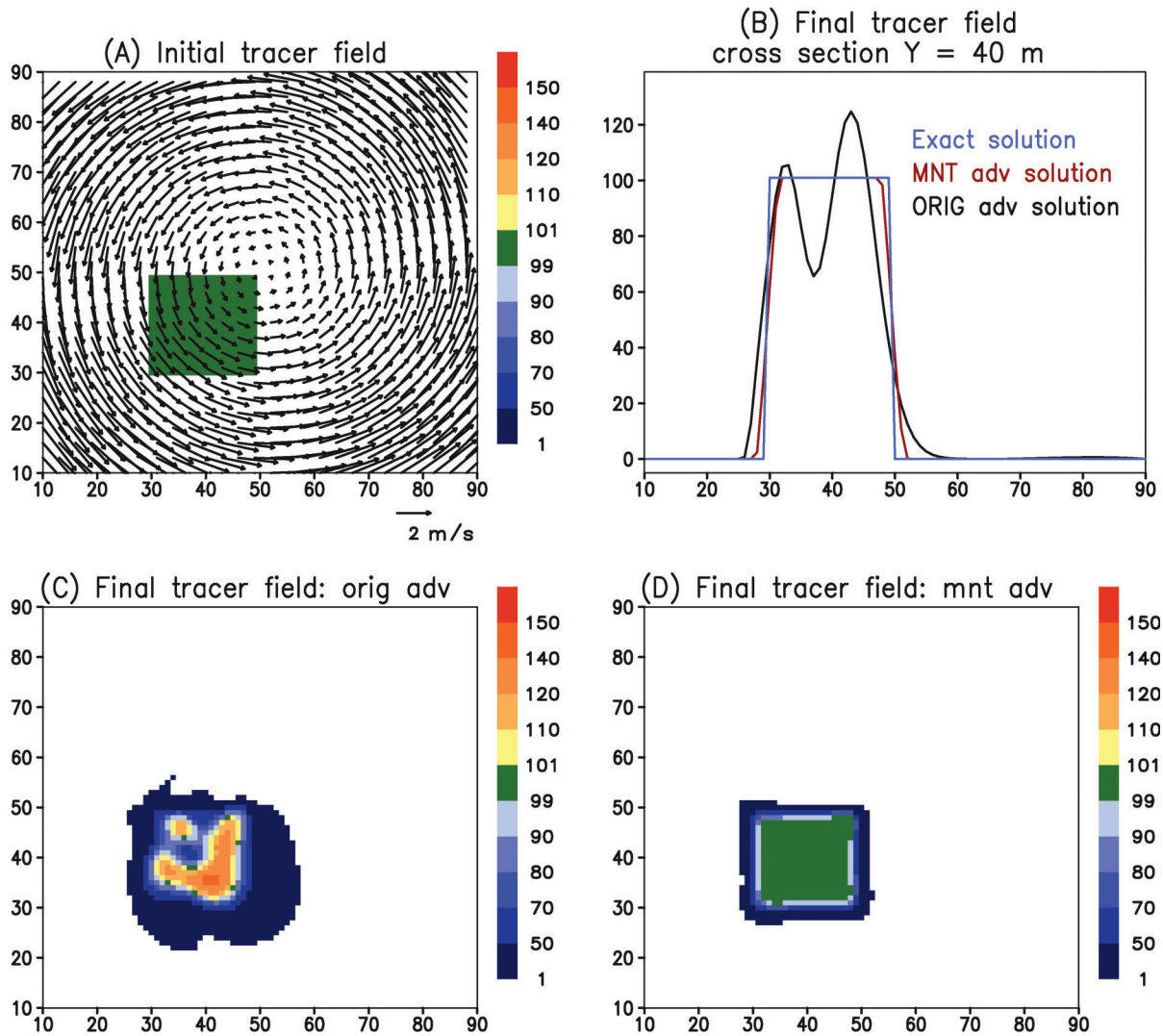


**Figure 1.** The rotational non-divergent flow test. (a) The initial tracer and wind fields. (b) Cross sections at grid box  $y=40$  m of the exact, orig and mnt solutions. (c) The numerical solution for the tracer mixing ratio after a full rotation using the orig advection scheme. (d) Same as Figure 1c but using the mnt advection scheme. The tracer fields are multiplied by 40000 for clarity of the color bar.

distributions are used, as seen at the top of Figures 2 and 3. The values of the first two tracer fields (square and slot) are defined as 100 au and its initial location is depicted in green in these figures; both are advected on a background of 20 au, shown in white. The triangular tracer fields have a maximum value of 100 au at the centers, decreasing linearly to 20 au at the bases, which covers 20 grid boxes. The Gaussian tracer fields also have a maximum value of 100 au at their centers, which are located at the points (50, 25) and (50, 75), decreasing exponentially to 20 au at their bases, which cover 20 grid boxes. The triangular and Gaussian tracer fields are also advected over a background of 20 au. Appendix A contains the exact equations for the initial conditions.

Figure 2 shows the tracer fields at time  $t = T/2$ , when the extreme deformation occurs. On the left side, the numerical solutions provided by the orig scheme are depicted. For

Figures 2a and 2c, overshoots of the tracer field greater than 30% of the maximum allowed value (100 au) are generated, as well as undershoots below 20 au, the minimum value allowed. Note also the oscillatory behavior of the tracer field indicated by alternation between blue and white. The solutions provided by the mnt scheme (Figures 2b and 2d) are much better. Overshoots or undershoots are not produced, nor oscillatory behavior of the tracer field. The numerical solution remains between 20 and 100 au. For the triangular and Gaussian tracer fields, the orig scheme does not produce overshoots (Figures 2e and 2g), but undershoots and oscillatory behavior are seen. Also, the numerical diffusion intrinsic in the orig scheme smoothes its solution, reducing the maximum simulated values. The mnt scheme provides a much improved numerical solution for the same cases. As before, overshoots or undershoots are not produced, nor the oscillatory behavior of the tracer field. The intrinsic

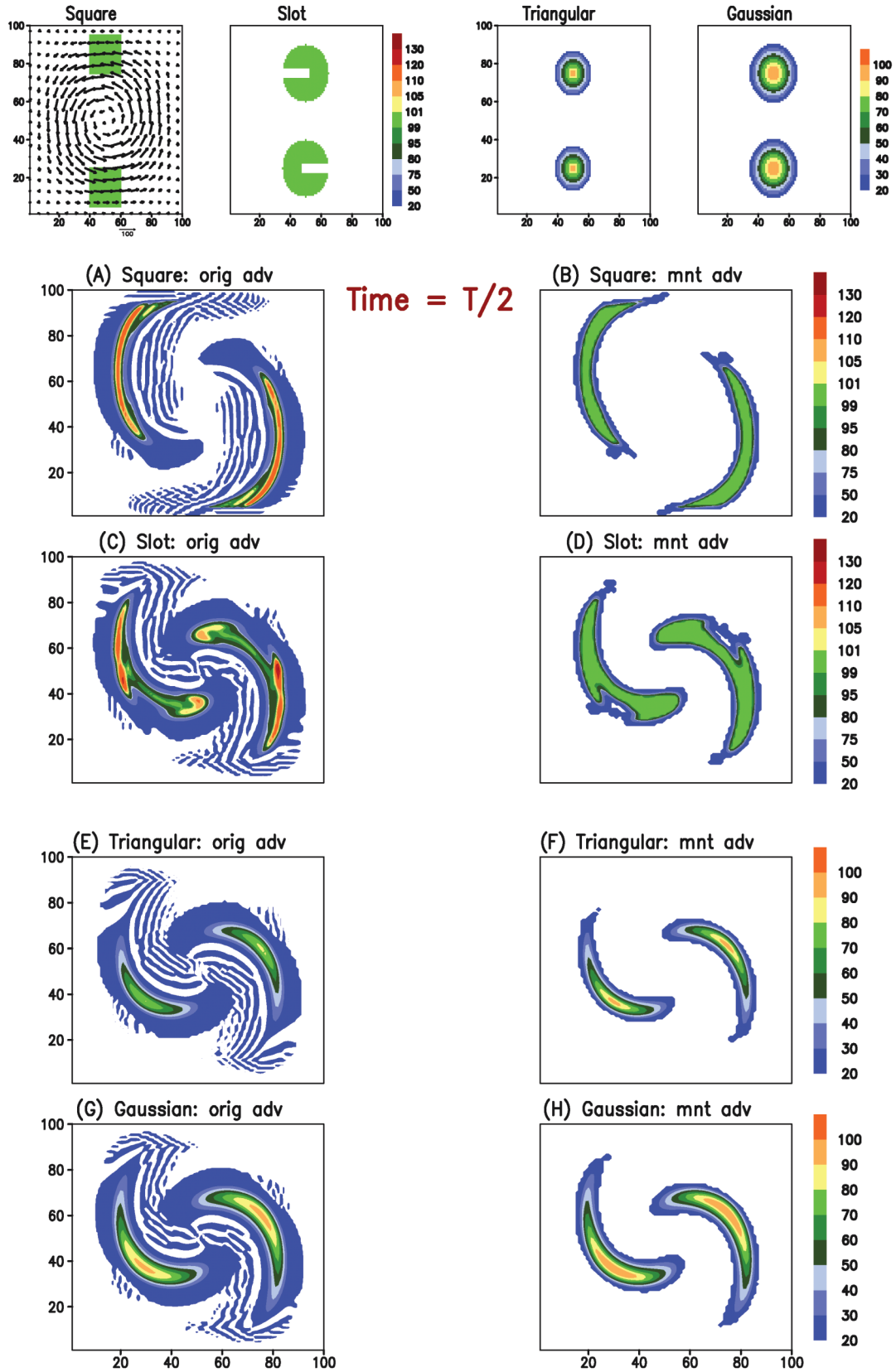


**Figure 2.** The non-divergent deformational wind flow test. (top) The four initial tracer fields to be advected. On the left side, the initial wind field appears. (a, c, e, g) The numerical solutions at time  $t = T/2$  using the orig scheme and (b, d, f, h) the numerical solutions at time  $t = T/2$  using the mnt scheme.

numerical diffusion is much lower and maximum simulated values are much closer to what is expected.

Figure 3 shows the tracer fields at time  $t = T$ , when the tracer is brought back to its initial position and the exact solution is known, once it is exactly equal to the tracer field at time  $t = 0$ . The eight (A, B, ..., H) simulated tracer distributions can be directly compared with the corresponding exact solutions shown Figure 3 (top). For the square and slot distributions, oscillatory and non-monotonic behaviors are evident in the orig scheme solutions (Figures 3a and 3c). In the mnt solutions (Figures 3b and 3d), these behaviors do not take place. Note also that the simulated shapes at time  $t = T$  by the mnt scheme resemble the initial condition much better than solutions provided by the orig one. For the triangular and Gaussian tracer distributions, once more, oscillatory and non-monotonic behaviors are shown by the orig scheme (Figures 3e and 3g), but not by the mnt one (Figures 3f and 3h). In these previous two cases, the much stronger numerical diffusion associated with the orig scheme is clearly evident. See Animation S1 in the auxiliary material<sup>1</sup> for a time evolution of the transport of the four tracers, from time  $t = 0$  and  $T$  with 10-minute interval.<sup>1</sup> The features described before are also depicted in Figure 4, which shows a cross section of tracer mixing ratio in au at time  $t = T$  and coordinate  $X = 50$  for the initial shapes in the form of a square (Figure 4a), slot (Figure 4b), triangular (Figure 4c) and Gaussian (Figure 4d). The exact solution is shown in blue, red depicts the mnt solution and the orig solution is in black. As discussed before, non-monotonic and oscillatory features are evident from the orig solution, as seen in Figures 4a and 4b, while the stronger numerical diffusion of this scheme is noticeable in Figures 4c and 4d. Note also that the mnt solution for the Gaussian distribution is almost perfect (Figure 4d), and the triangular one shows only a small deviation very close to the center of the tracer field.

A further evaluation of the numerical performance of both schemes is shown in Table 3. Note that for single precision and a total mass of the order of  $10^4$ , which is the case for the experiments in this section, the machine precision is around  $10^{-5}\%$ . Mass conservation is in the machine precision range in both schemes. However, for the global standard errors, the mnt scheme shows much better scores, in some cases 4 to 5 times better.

### 3.1.3. Deformational Divergent and Time-Dependent 2-D Wind Flow

In this section, we set a periodic time-dependent and divergent 2-D wind field, also recommended by NL2010:

$$\begin{cases} u(x,y,t) = -U_0 \sin^2(a\pi x) \sin(2a\pi y) \cos(\pi t/T) \\ v(x,y,t) = +\frac{U_0}{2} \sin(2a\pi x) \cos(a\pi y) \cos(\pi t/T). \end{cases} \quad (20)$$

<sup>1</sup>Auxiliary materials are available in the HTML. doi:10.1029/2011MS000084

Similar to the previous case, the flow field  $(u,v)$  reverses after time  $t = T/2$  and then brings the tracer field back to its initial shape at time  $t = T$ , providing the exact solution to evaluate the numerical one. It can be shown that, in general,  $\nabla \cdot (u,v)^T \neq 0$ . All parameters shown in equation (20) are the same as those employed in equation (19) of the previous test case, as well as the grid configuration. However, only the mnt scheme is studied with this wind flow.

This case is more difficult to implement because the air density is no longer constant in time and space, due the compression and decompression provoked by this kind of wind flow. So, the mass continuity equation (equation (2)) for the dry air density has to be solved simultaneously with equation (3). To solve the dry air mass continuity equation, we use the splitting operator technique. In this case, equation (2) is rewritten in the following form

$$\frac{\partial \rho_a}{\partial t} = \left( \frac{\partial \rho_a}{\partial t} \right)_{adv} + \left( \frac{\partial \rho_a}{\partial t} \right)_{div}, \quad (21)$$

and split in two as shown in equation (22)

$$\begin{cases} \left( \frac{\partial \rho_a}{\partial t} \right)_{adv} = -\vec{v} \cdot \nabla \rho_a & (22a) \\ \left( \frac{\partial \rho_a}{\partial t} \right)_{div} = -\rho_a \nabla \cdot \vec{v} & (22b) \end{cases}$$

A time step of 5 seconds was needed to integrate equation (21). After calculating  $\nabla \cdot (u,v)^T$  using equation (20) and inserting it in equation (22b), it becomes an ordinary 1<sup>st</sup> order differential equation, which can be integrated in time using a semi-implicit scheme. The initial condition is  $\rho_a(t=0) = 1 \text{ kg m}^{-3}$ . After this step, the dry air density is updated, but only from the contribution of local wind divergence. Then, the W2000 scheme is used to integrate equation (22a), providing the complete solution for equation (21).

As defined in the previous section,  $U_0$  is the amplitude of each wind component, in this case 80 m/s, the parameter  $a$  is  $\pi/1000 \text{ km}^{-1}$  and  $T = 6 \text{ h}$  is the time period. The integration of the advection equation was performed with 10 km grid spacing in each direction with the model domain composed of  $100 \times 100$  grid boxes. The time step was the same as that used to integrate equation (21), which corresponds to 0.04 for the maximum CFL number. Figure 5 shows the time evolution of the tracer mixing ratio and density of a Gaussian distribution (see Appendix A) under the divergent deformational flow described by equation (20). Figures 5a and 5b show the distribution at the initial time. At this time, the maximum values for mixing ratio and density are 100 kg/kg and  $100 \text{ kg/m}^3$ , respectively. The tracer distributions at time  $t = T/2$ , when the extreme deformation occurs, are shown in Figures 5c and 5d. It can be noted that spurious oscillations are not produced, and there is monotonic preservation of the mixing ratio field. Also at this time, the density field reaches values of up to  $200 \text{ kg/m}^3$ , higher

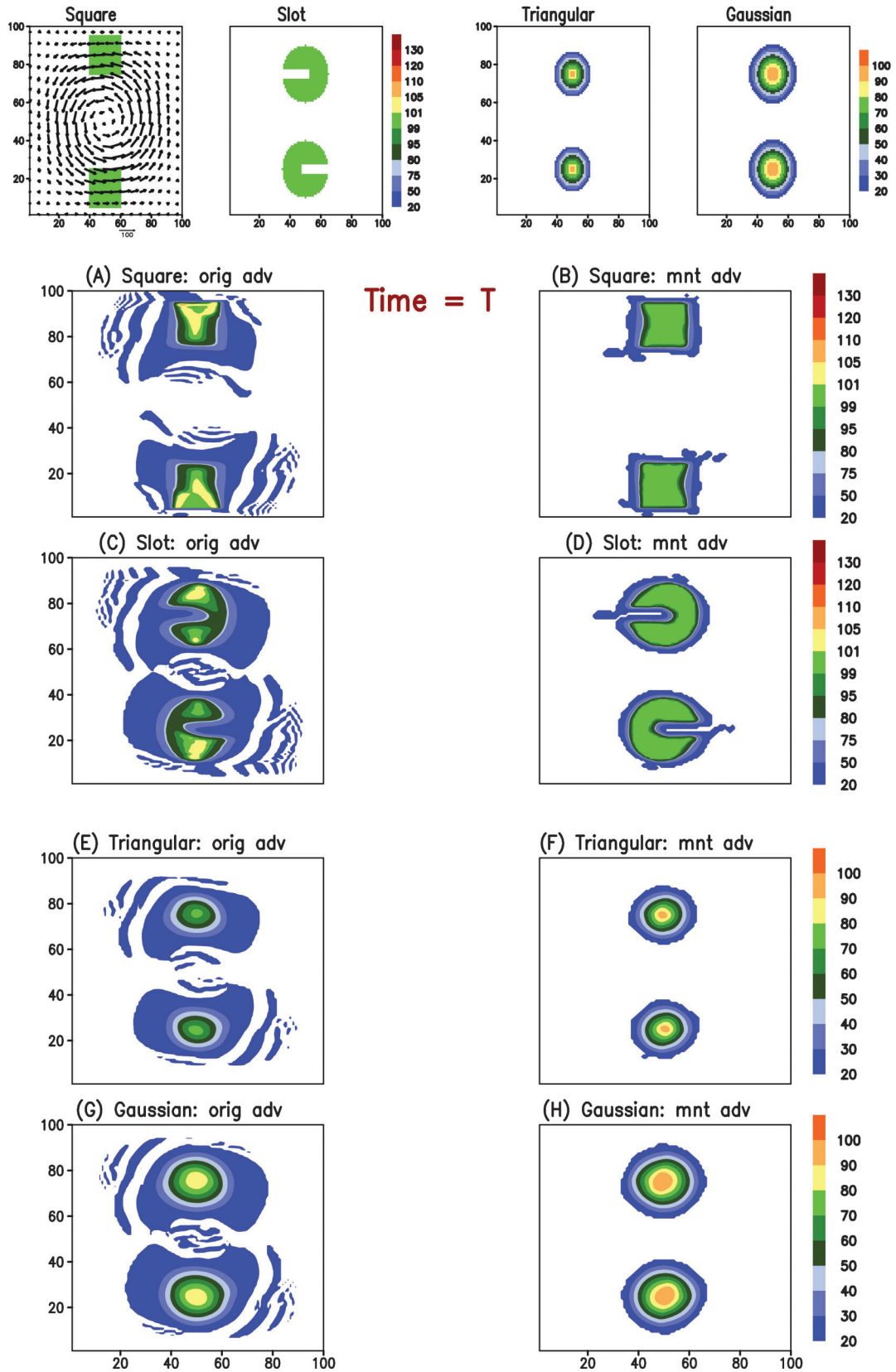


**Figure 3.** The non-divergent deformational wind flow test. (top) The four initial tracer distributions to be advected are shown. On the left, the initial wind field also appears. (a, c, e, g) The numerical solutions using the orig scheme at time  $t = T$ , when the tracer patterns return back to their initial position and shape. (b, d, f, h) The same as before but for the mnt scheme.

than the maximum value present in the initial condition. This behavior is expected because of the strong compression zones existing in this wind flow. At time  $t = T$ , when the tracer is brought back to its initial position and shape (Figures 5e and 5f), both fields present very similar patterns to the exact solutions.

### 3.1.4. Tracer Correlations

Some authors [e.g., *Plumb and Ko, 1992; Plumb, 2007*] have shown the existence of certain long-lived species in the stratosphere for which the concentrations are interrelated. In this case, a scatter plot of the mixing ratio of one versus that of the other collapses into a well defined curve. *Lin and Rood [1996]* advocated that a transport model must be able to maintain the existing correlation information among the chemical species. In this section we follow *Lauritzen et al. [2011]* for testing the preservation of tracer correlations by both advection schemes. Maintenance of linear or non-linear (quadratic and fourth order) correlations existing at

the beginning is tested under a deformational non-divergent and time-dependent 2-D wind flow given by equation (19). The tests make use of the same grid configuration and time step as in Section 3.1.2. We define a tracer field  $Tr_1$  given by the Gaussian distribution described in that section and shown at the top of Figure 2. Three additional tracer fields are defined following the relationships

$$\begin{cases} Tr_2 = a_1 Tr_1 + b_1 & (23a) \\ Tr_2 = a_2 Tr_1^2 + b_2 & (23b) \\ Tr_2 = a_4 Tr_1^4 + b_4, & (23c) \end{cases}$$

where  $a_i$  and  $b_i$  are constants. For these tests, the constants used were  $a = \{3/2, 3/200, 3/160000\}$  and  $b = \{22, 32, 12\}$ . Scatter plots of the mass mixing ratio of two interrelated tracers  $Tr_1$  and  $Tr_2$  are shown in Figure 6. In all panels, the blue dots represent the initial correlation existing between the mixing ratios of two tracers. The scatter plots for time  $t = T/2$ , when the extreme deformation occurs, are shown in Figures 6a–6c, while the results corresponding to time  $t = T$ ,

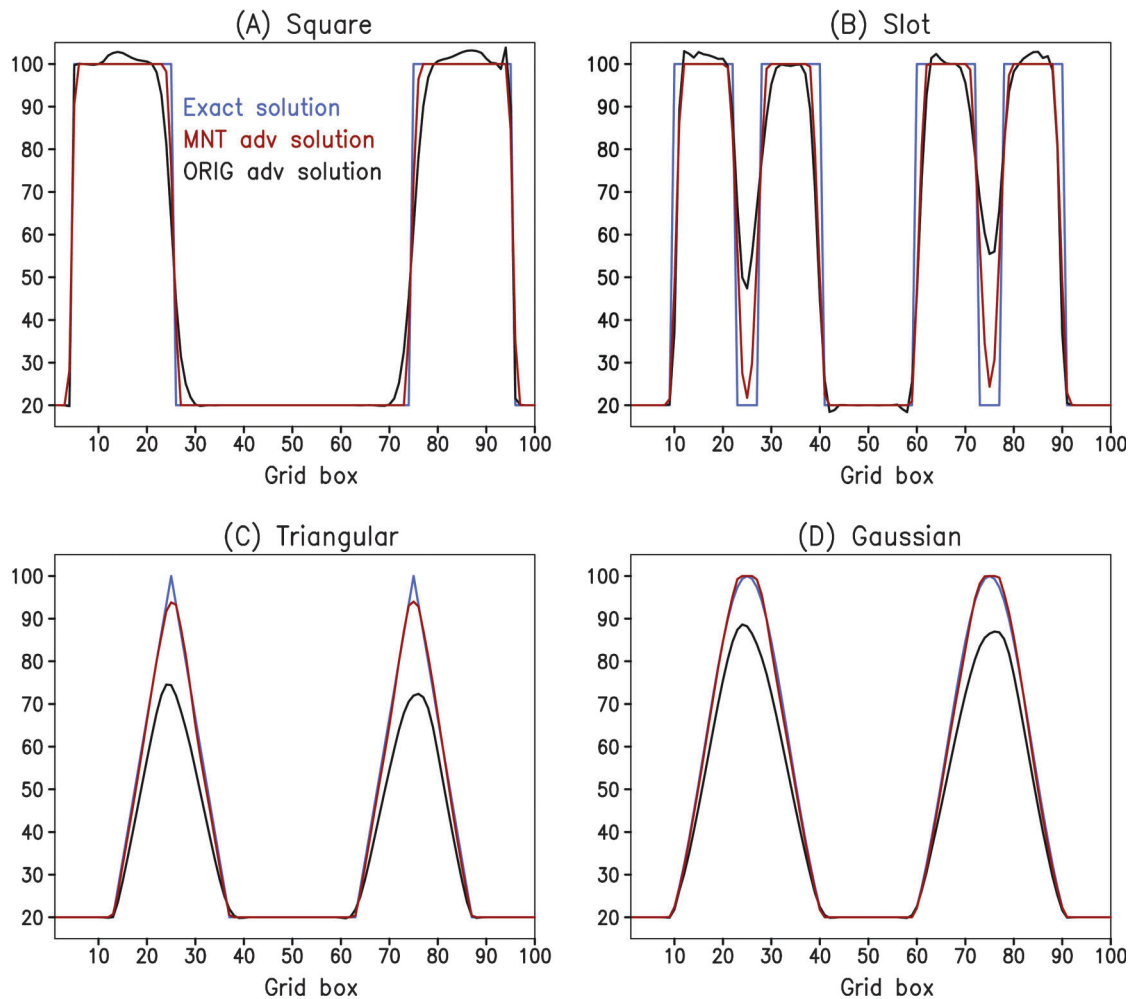


**Figure 4.** Cross section at grid box  $X=50$  of the mixing ratio at time  $t = T$ , when the tracer patterns return back to their initial position. The exact, orig and mnt solutions are shown for the initial shape given by a (a) square, (b) slot, (c) triangular, and (d) Gaussian.

**Table 3.** The Normalized Standard and Mass Conservation Errors for the Deformational Non-divergent Wind Flow Test Described by Equation (19)<sup>a</sup>

Initial Shape of the Tracer Field	$l_1$ orig	$l_1$ mnt	$l_2$ orig	$l_2$ mnt	$l_\infty$ orig	$l_\infty$ mnt	$m_{err}$ (%) orig	$m_{err}$ (%) mnt
Square	0.083	0.046	0.212	0.163	0.548	0.480	$1 \cdot 10^{-4}$	$8 \cdot 10^{-5}$
Slot	0.131	0.057	0.249	0.170	0.631	0.613	$-7 \cdot 10^{-5}$	$8 \cdot 10^{-5}$
Triangular	0.034	0.008	0.082	0.025	0.220	0.059	$6 \cdot 10^{-5}$	$-8 \cdot 10^{-5}$
Gaussian	0.033	0.009	0.106	0.030	0.246	0.071	$-9 \cdot 10^{-5}$	$-7 \cdot 10^{-6}$

<sup>a</sup>The quantities correspond to time  $t = T$ , when the tracer patterns return back to their initial position and the exact solution is then known.

when the tracer patterns return back to their initial position and shape, are shown in Figures 6d–6f. The results of the orig and mnt schemes are depicted in black and red, respectively. As shown in Figures 6a and 6d, both schemes precisely maintain the linear correlation. However, for the two prescribed non-linear correlations (Figures 6b, 6c, 6e, and 6f), the orig scheme shows a damping of the maximum mixing ratio and its dots populate the concave side of the blue ‘curve’. P. H. Lauritzen and J. Thuburn (Evaluating advection/transport schemes using interrelated tracers, scatter plots and numerical mixing diagnostics, submitted to *Quarterly Journal of the Royal Meteorological Society*, 2011) introduced a schematic classification of the numerical mixing which results from advection schemes. According to this classification, the behavior of the orig scheme is referred to as ‘real’ mixing because it resembles a true mixing caused by physical mechanisms. On the other side, the dots associated with the mnt scheme fall closely around the blue ‘curve’, indicating much better preservation of the non-linear correlations. In addition, the damping is much smaller than that produced by the orig scheme. Following Lauritzen and Thuburn (submitted manuscript, 2011), the mnt scheme presents one aspect of ‘real’ mixing associated with the red dots on the concave side of the blue ‘curve’, but also another one referred to as ‘range-preserving unmixing’ due to the red dots which populate the convex side of the ‘curve’, but do not create overshoots. The term ‘unmixing’ is used to characterize the up-gradient transport caused by purely numerical reasons. The fact that both advection schemes do not precisely preserve the non-linear correlations is consistent with the work of Thuburn and McIntyre (1997). In this paper, the authors demonstrated that no Eulerian advection schemes can preserve non-linear correlations.

### 3.1.5. Multiple Versus Individual Component Property Preservation

In this section, we address the problem of the how well the global properties of a multi-component system are preserved when each tracer which makes up the system is transported by both advection schemes. The motivation for this study is due to the fact that the constraints and flux limiters imposed by advection schemes to accomplish the monotonic condition deviate them from being strictly linear.

In the first test, three tracer fields in which the sum of the mixing ratios is a constant are advected by both schemes. Both

the orig and mnt schemes strictly achieve the preservation of constancy (see Section 2). So, here the test consists of applying both advection schemes to transport the three tracers and checking if the sum of their mixing ratios stay constant at all times. The three tracer fields are defined as Gaussian distributions being transported by a deformational, non-divergent and time-dependent 2-D wind flow given by equation (19). The sum of the mixing ratio of the three tracers is initially defined as 360 au (see Appendix A for the exact initial conditions for all the tracers used in this section). The tests make use of the same grid configuration and time step as Section 3.1.2. Figures 7a and 7b show the results for the orig and mnt advection schemes, respectively, and correspond to the mixing ratio cross section at grid box  $Y = 50$  at time  $t = T$ , when the tracer patterns return back to their initial position and shape. Figure 7a shows the results for the orig advection. As the reader can see, the numerical solution presents significant differences from the exact solution for the tracers  $Tr_1$ ,  $Tr_2$  and  $Tr_3$ ; however, the sum  $Tr_1+Tr_2+Tr_3$  is perfectly preserved, indicating that this scheme keeps the linear property of the advection equation. However, the results from the mnt advection (Figure 7b) are much better when comparing the numerical solution with the exact one of each tracer. But, the sum  $Tr_1+Tr_2+Tr_3$  is not well preserved as in the case of the orig advection. This denotes that the mnt scheme introduces a small non-linearity in the originally linear problem. This characteristic of the Walcek scheme was already discussed by Ovtchinnikov and Easter [2009]. However, as stated by Lauritzen and Thuburn (submitted manuscript, 2011), schemes with shape-preserving filters will, in general, not be able to preserve the sum when transporting the tracers individually. They show also that even highly accurate advection algorithms like the conservative semi-Lagrangian multi-tracer transport scheme (CSLAM [Lauritzen et al., 2010]) do not preserve the sum, if its shape-preserving filters are used.

In the second test, four Gaussian tracer fields ( $Tr_1, \dots, Tr_4$ ) are advected under the same wind flow described before. The 4<sup>th</sup> tracer has a mass mixing ratio given by  $Tr_4 = Tr_1+Tr_2+Tr_3$  (see Appendix A). Figures 7c and 7d show the results for the orig and mnt schemes, respectively, at time  $t = T$ . The numerical solutions of the orig scheme present large differences from the exact solution for the tracers  $Tr_1$ ,  $Tr_2$ ,  $Tr_3$  and  $Tr_4$  (the numerical solution for this tracer is exactly the same as that represented by the green line, which is the sum  $Tr_1+Tr_2+Tr_3$ ). As before, the sum ( $Tr_1+Tr_2+Tr_3$ ) and  $Tr_4$  are almost the same, indicating the linearity preservation of

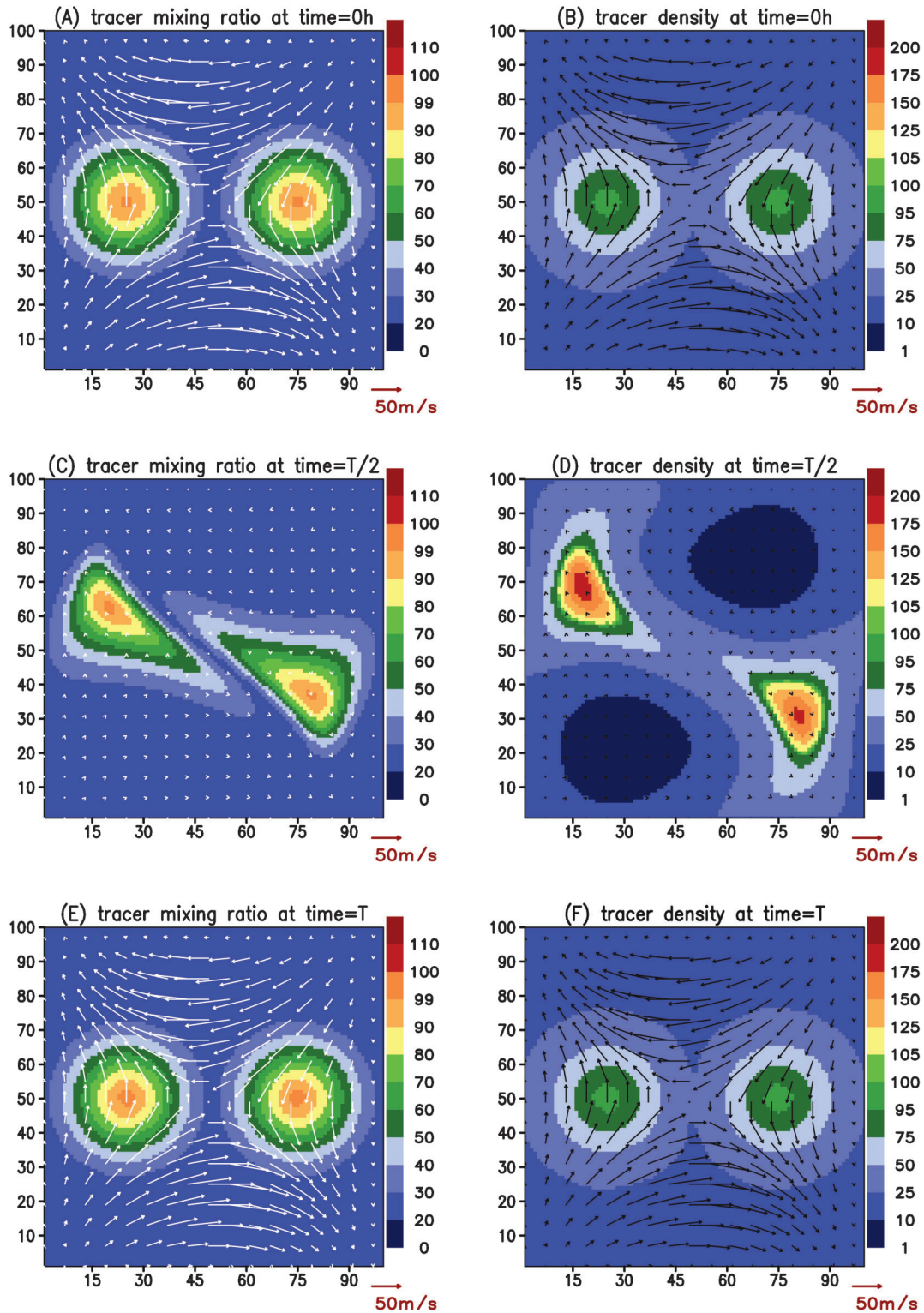


**Figure 5.** The divergent deformational flow test applied with a Gaussian distribution. Only results with the mnt scheme are shown. (a) The tracer concentration field expressed in terms of the mass mixing ratio at the initial time. (b) Same as Figure 5a but in terms of mass density. Both fields have maximum values of 100 kg/kg and 100 kg/m<sup>3</sup>, respectively. (c, d) The numerical solutions at time  $t = T/2$ , the time of the extreme deformation and (e, f) the solutions at time  $t = T$ , when the tracer patterns return back to their initial position and shape.

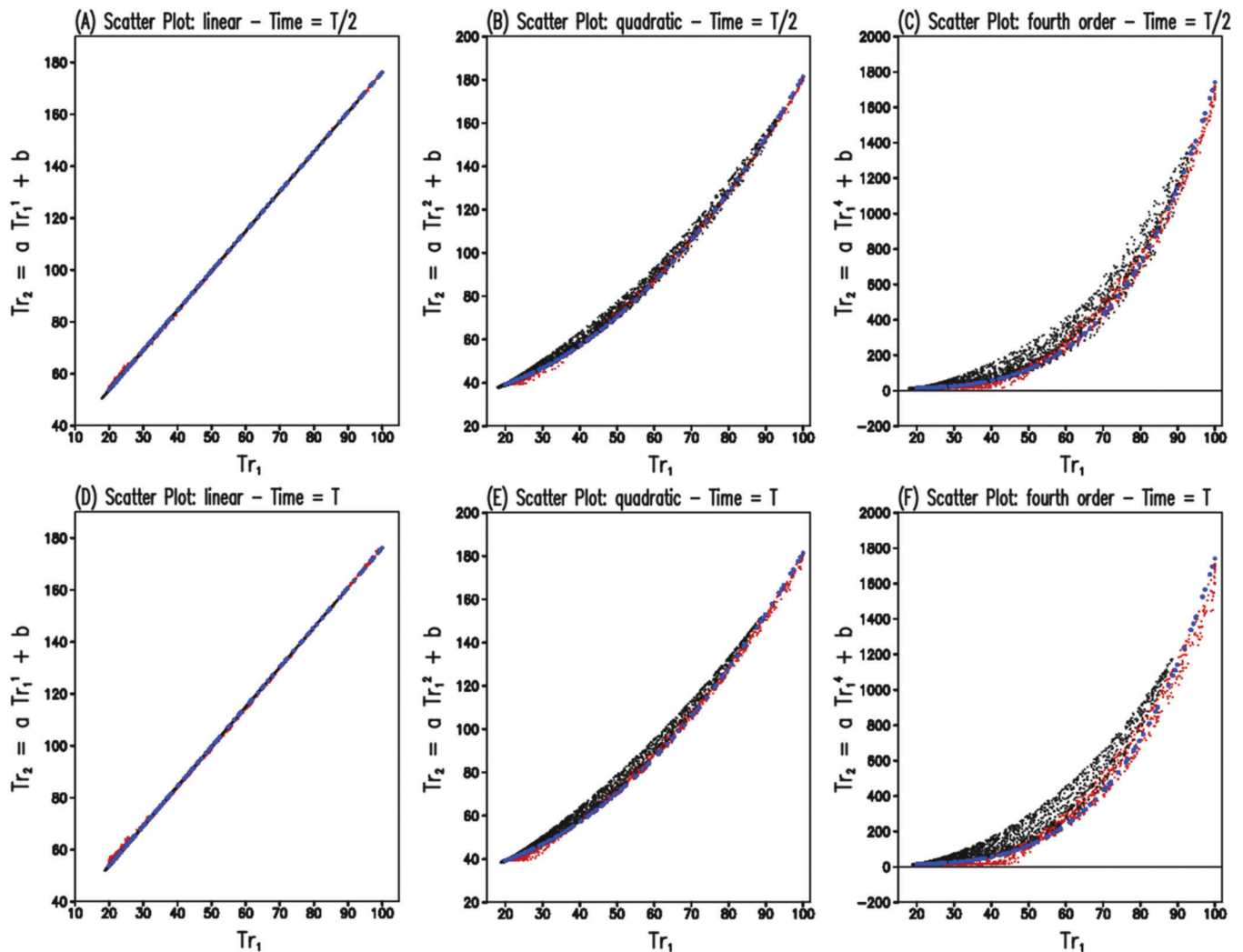


**Figure 6.** Scatter plots of the mixing ratio of two interrelated tracers transported by a deformational non-divergent and time-dependent 2-D wind flow. The blue dots represent the initial correlation existing between the mixing ratios of the two tracers. Initial linear, quadratic and fourth order correlations are tested with the orig (black) and mnt (red) advection schemes. (a–c) The results at time  $t = T/2$ , when the extreme deformation occurs. (d–f) The correlations at time  $t = T$ , when the tracers patterns return back to their initial position and shape.

the orig scheme. The numerical results from the mnt scheme (Figure 7d) are much better and the sum  $Tr_1 + Tr_2 + Tr_3$  is very close to both  $Tr_4$  and the exact solution.

The error quantification for the second test is described in Table 4. Again, for the global standard errors, the mnt scheme shows much better scores, in some cases 4 to 5 times better.

### 3.2. Some Examples of Real Cases

#### 3.2.1. Advection of a Rectangular Parallelepiped Tracer Field by a Realistic 3-D Wind Flow

Here we transport an idealized tracer field (in this case, a rectangular parallelepiped) under a realistic 3-D wind flow simulation. Real simulation of the wind field is obtained by using initial and boundary conditions from the Brazilian

Center for Weather Prediction and Climate Studies (CPTEC) analysis fields using a T126L28 resolution (the approximate grid spacing is 100 km and more details are provided in the next section) and full model physics. The model was configured with one grid with 10 km horizontal resolution on a polar-stereographic projection covering the southeast part of Brazil ( $120 \times 120$  horizontal grid points denoted by the indexes X and Y) and with a time step of 15 seconds. Since the grid covers a small domain and the center of the plane of projection is located in the center of the grid, the true grid spacing is very close to 10 km. The vertical coordinate is a terrain following coordinate and its resolution varies telescopically, with higher resolution at the surface (100 m) with a ratio of 1.09 up to a maximum vertical resolution of 950 m, with the top of the model at 23 km (a total of 42 vertical levels). The total length of the

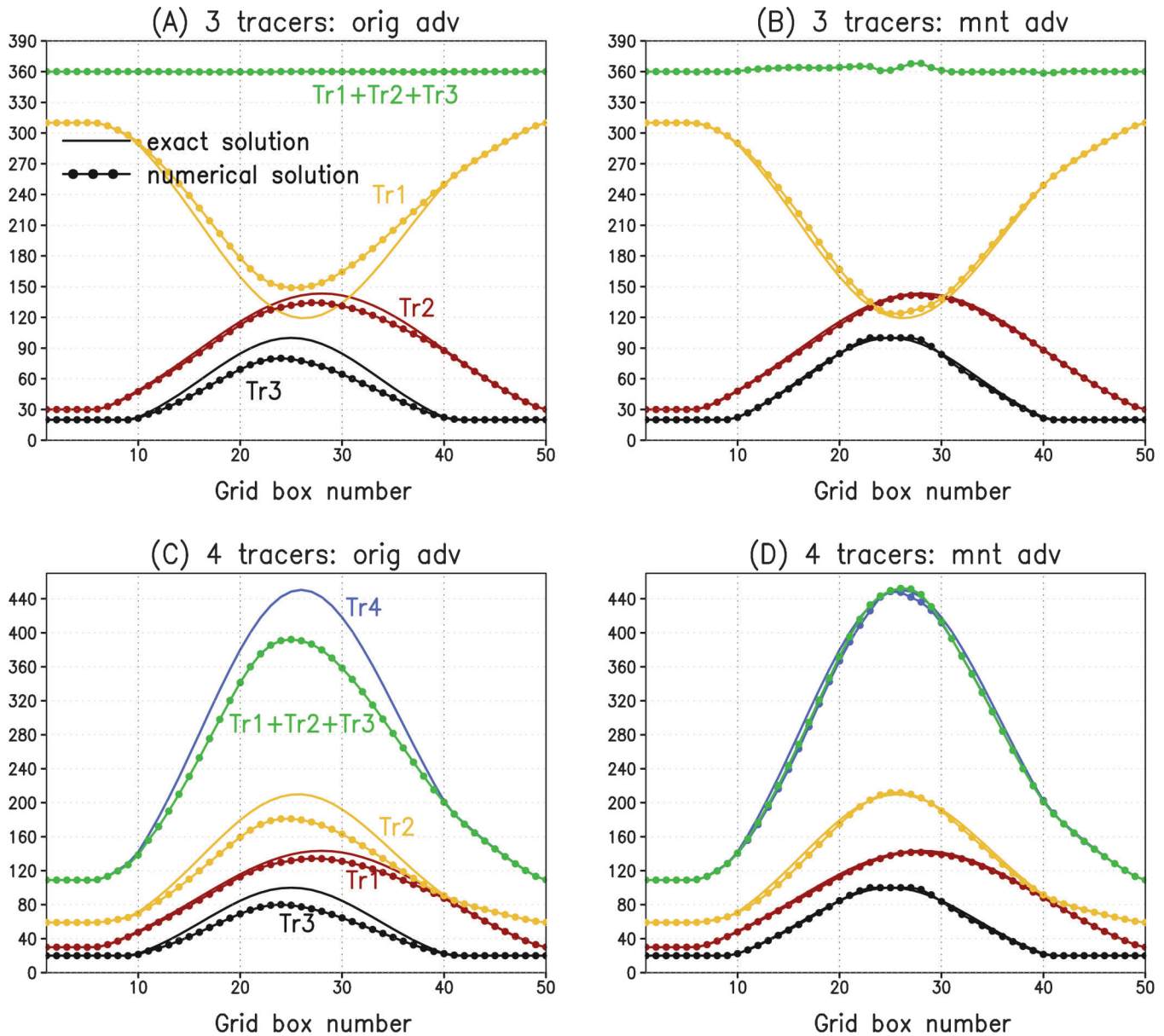


**Figure 7.** Multicomponent transport simulations using the orig and mnt schemes. (a, b) The cross sections at grid box  $Y=50$  of the mixing ratio of 3 interrelated tracers at time  $t = T$ . (c, d) The same as before, but for the 4 tracers case.

time integration was 24 hours. The tracer mixing ratio is initiated with 100 au and the background is set to zero. The horizontal domain initially occupied by the tracer was  $10 <$

**Table 4.** The Normalized Standard Errors for the Deformational Non-divergent Wind Flow Test Described by Equation (19) and for the Four Tracers Described in Figures 7c and 7d<sup>a</sup>

Tracers	$l_1$ orig	$l_1$ mnt	$l_2$ orig	$l_2$ mnt	$l_\infty$ orig	$l_\infty$ mnt
$Tr_1$	0.044	0.010	0.091	0.028	0.139	0.058
$Tr_2$	0.036	0.016	0.057	0.027	0.086	0.048
$Tr_3$	0.025	0.009	0.048	0.019	0.094	0.046
$Tr_4$	0.028	0.011	0.051	0.021	0.090	0.048
$Tr_1+Tr_2+Tr_3$	0.028	0.010	0.051	0.019	0.091	0.042

<sup>a</sup>The quantities correspond to time  $t = T$ , when the tracer patterns return back to their initial position and the exact solution is known.

$X < 30$  and  $10 < Y < 30$ , while in the vertical the tracer was initially localized between 1.7 and 4.1 km in height. Figures 8a and 9a show the initial horizontal and vertical locations of the tracer field, respectively. The tracer distributions 12 hours after and simulated by the orig and mnt schemes are shown in Figures 8c and 8d, respectively. The orig scheme clearly introduces spurious oscillations, overshoots and undershoots. Also, stronger horizontal diffusion is evident. On the other hand, the simulation produced by the mnt scheme is much better at keeping the monotonicity of the distribution without the spurious oscillations. Figure 8b shows the cross section of the tracer fields at time 0 and 12 h at latitude 25.8 S. From this figure, the monotonic preservation of the mnt scheme is evident. The

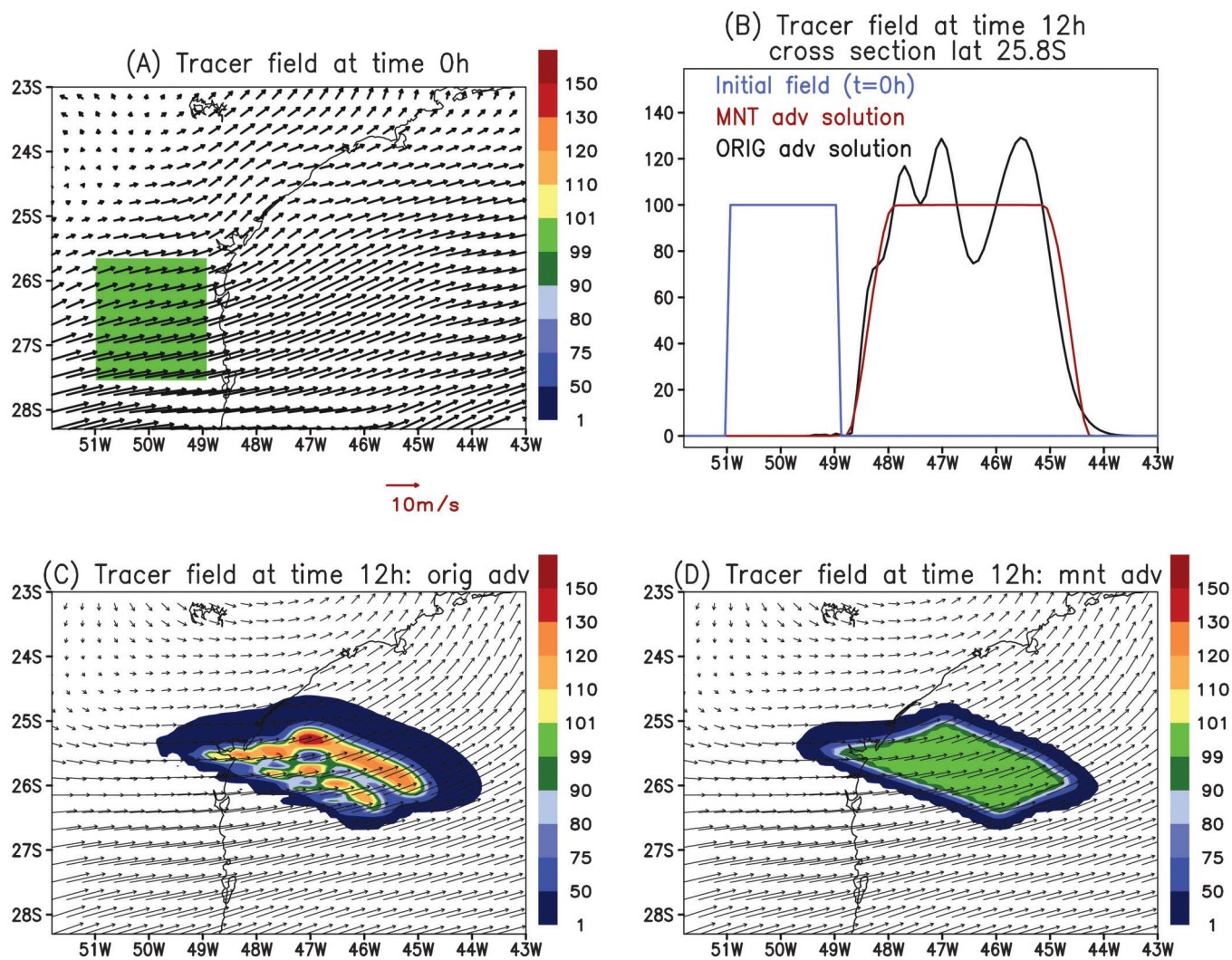


**Figure 8.** A 3-D real case study: transport of a rectangular parallelepiped by a realistic divergent flow. (a) The tracer concentration field expressed in terms of mass mixing ratio at initial time and a height of 1900 m; the horizontal wind flow is also depicted. (b) The cross section of the tracer mixing ratio at latitude 25.8 S. The initial cross section (blue) as well as the one simulated by the mnt (red) and orig (black) schemes at 12 hours are shown. (c) The mass mixing ratio after 12 hours and using the orig advection scheme. (d) Same as Figure 8c but with the mnt scheme.

quality of vertical transport can be evaluated from Figure 9. As before, Figures 9c and 9d show the tracer distributions 12 hours after and simulated by the orig and mnt schemes, respectively. A similar discussion applies here. Observe the strong under- and overshoots produced by the orig scheme as showed by Figure 9b. In general, the quality of the results with the mnt scheme is remarkable.

Medvigy et al. [2005] showed that the RAMS model in its native formulation exhibits a significant degree of mass non-conservation associated with the approximated equation used to predict the air pressure, which is done in terms of the Exner function. They improved the mass conservation in RAMS by two orders of magnitude by extending the formulation to the exact, physically complete equation. This improvement is also included in the CCATT-BRAMS model and its impact together with the

new advection scheme is discussed as follows. Figure 10 shows the time evolution of the mass conservation error (%) calculated for the initial rectangular parallelepiped tracer field discussed in this section. Using the original RAMS formulation (denoted by IEXEV1), after 18 hours the errors are approximately 0.25 and 0.22% for the orig and mnt schemes. In our case, the use of Medvigy et al.'s [2005] extension (denoted by IEXEV2) reduced the errors to approximately 0.17 and 0.14%. These results show that the mnt advection itself produced an improvement on the RAMS mass conservation.

### 3.2.2. Vertical and Horizontal Transport Under an Intense Rainfall Regime

In this section, we explore the performance of the advection schemes in vertically transporting tracers from the PBL to

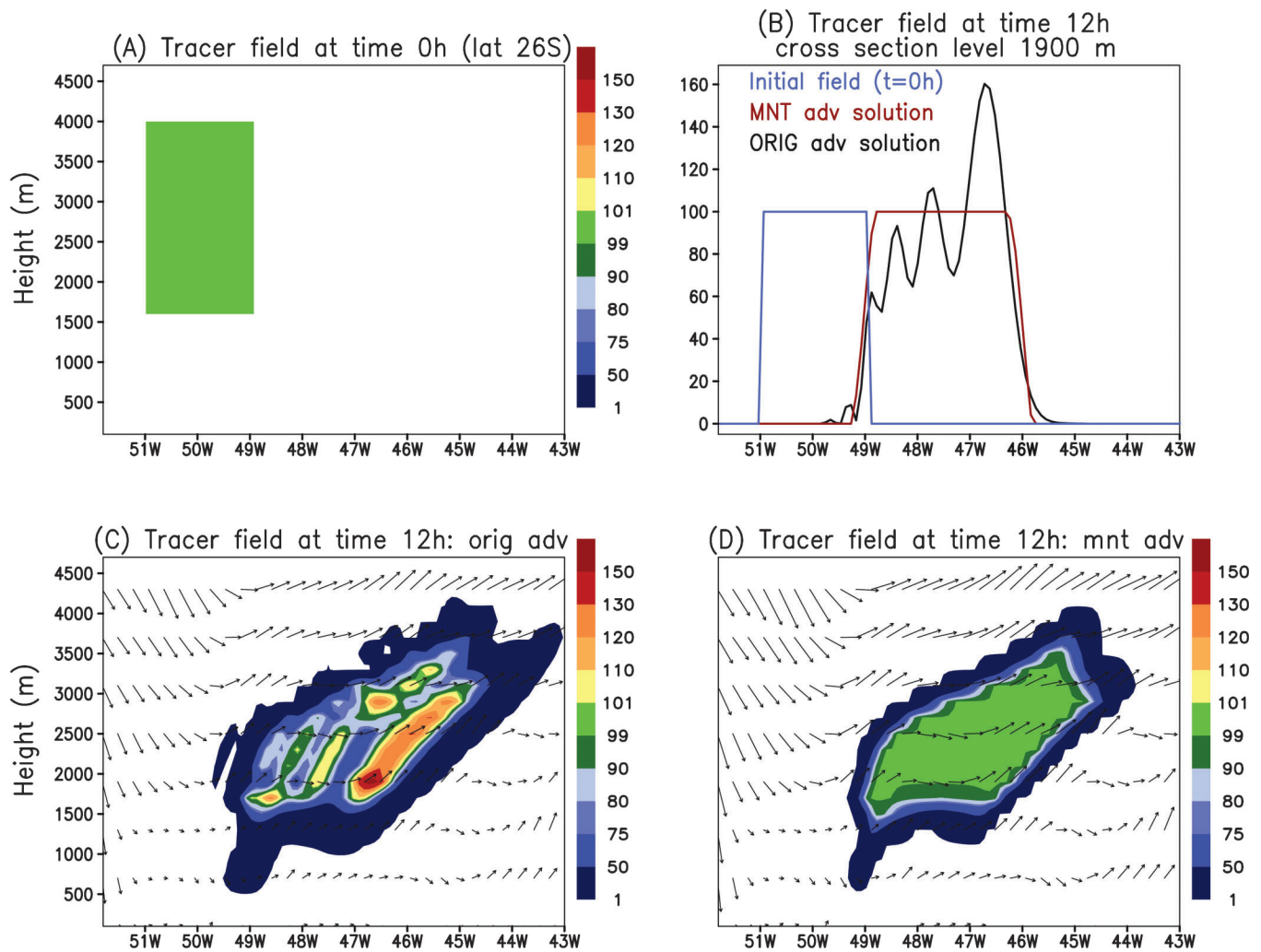


**Figure 9.** A 3-D real case study: transport of a rectangular parallelepiped by a realistic divergent flow. (a) The tracer concentration field expressed in terms of mass mixing ratio at initial time and latitude 26 S. (b) The cross section of the tracer mixing ratio at a height of 1900 m. The initial cross section (blue) as well as the ones simulated by the mnt (red) and orig (black) schemes at 12 hours is shown. (c) The mass mixing ratio after 12 hours and using the orig advection scheme. (d) Same as Figure 9c but with the mnt scheme. The wind fields depicted in Figures 9c and 9d correspond to the components  $u$  and  $w$ . The magnitude of the vertical velocity ( $w$ ) is multiplied by 1000 for clarity.

upper levels due the occurrence of convective systems and then the horizontal transport at these levels by the prevailing winds. We performed simulations for the time period of 8–9 August 2008, when a mid-latitude cold front approach produced intense rainfall over the southeast part of Brazil, a region characterized by densely populated urban areas with a massive amount of mobile and industrial emission sources. The model configuration was the same as in Section 3.2.1. The total length of the time integration was 2 days, starting on 8 August 2008 at 00 UTC. For the atmospheric initial and boundary conditions, the 6 hourly CPTEC T126L28 analysis fields of horizontal wind, geopotential height, air temperature and water vapor mixing ratio were used for the model initialization and to provide the necessary boundary conditions using a 4DDA (four-dimensional

data assimilation) nudging technique. Initial and boundary conditions for the chemical species were taken from the Multi-scale Chemistry and Transport Model (MOCAGE) [Peuch et al., 1999], also using the previously described nudging technique.

Figure 11a shows the 24-hour accumulated rainfall as estimated by remote sensing, with values up to 100 mm. The black box denotes the model domain. The corresponding model simulation is shown in Figure 11b. Observe that the model is able to capture several aspects of the remote sensing rainfall distribution, with accumulated rainfall up to 100 mm close to the estimated maximum. Here we will not discuss in details the model skill in the simulation of convective systems, but only the vertical and horizontal transport of tracer fields. The impact of the advection

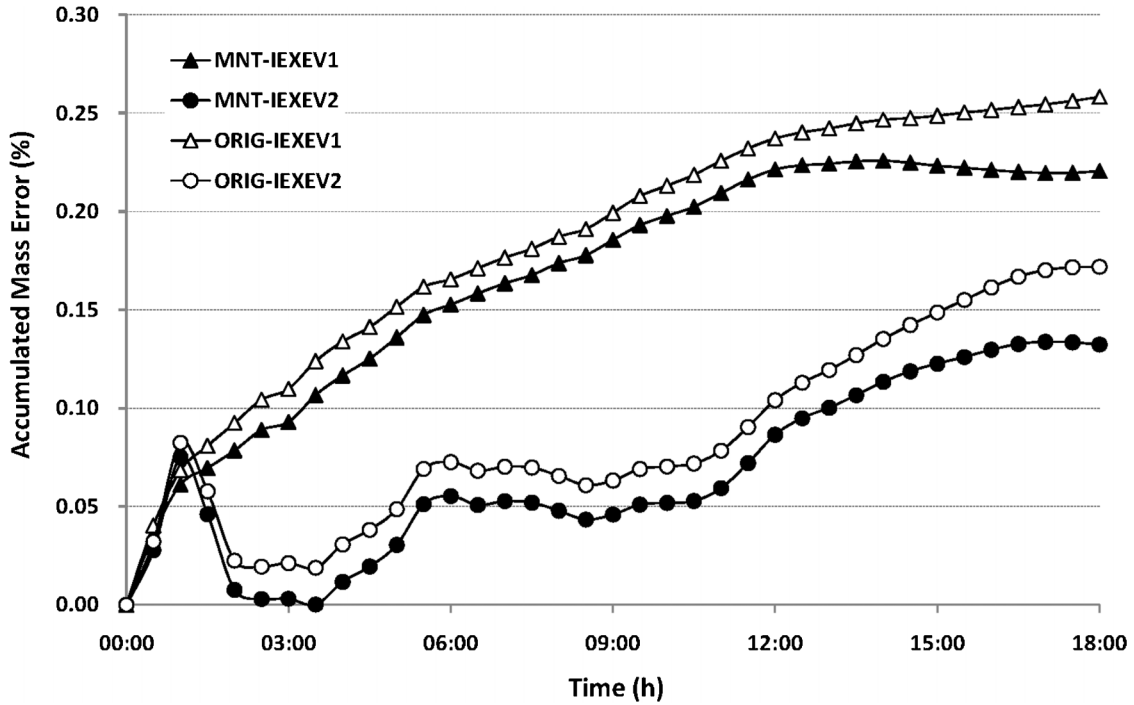


**Figure 10.** The time evolution of the mass conservation error (%) calculated for the initial rectangular parallelepiped tracer field being advected by a real 3-D wind flow. The index IEXEV1 refers to the simulation where the original RAMS formulation was used to prognosticate the air pressure, while IEXEV2 refers to *Medvigy et al.'s* [2005] extension using the exact, physically complete equation. Only results before 18 hours of simulation are shown, since after this time mass started to flow out of the model domain.

schemes on the vertical transport can be evaluated from Figure 12. Figures 12a and 12b refer to the simulation using the orig scheme but with different strengths of horizontal diffusion, which are applied to the dynamical as well as tracer variables, here represented by the user-specified parameter *akmin* (see Appendix B for details

about the RAMS horizontal diffusion). The simulation presented in Figure 12a has much stronger diffusion (*akmin* = 1) than the one in Figure 12b (*akmin* = 0.01). Using weak diffusion with the orig scheme (Figure 12b), spurious oscillations of the tracer field are produced, for example, in the first 3 km of height and around longitude

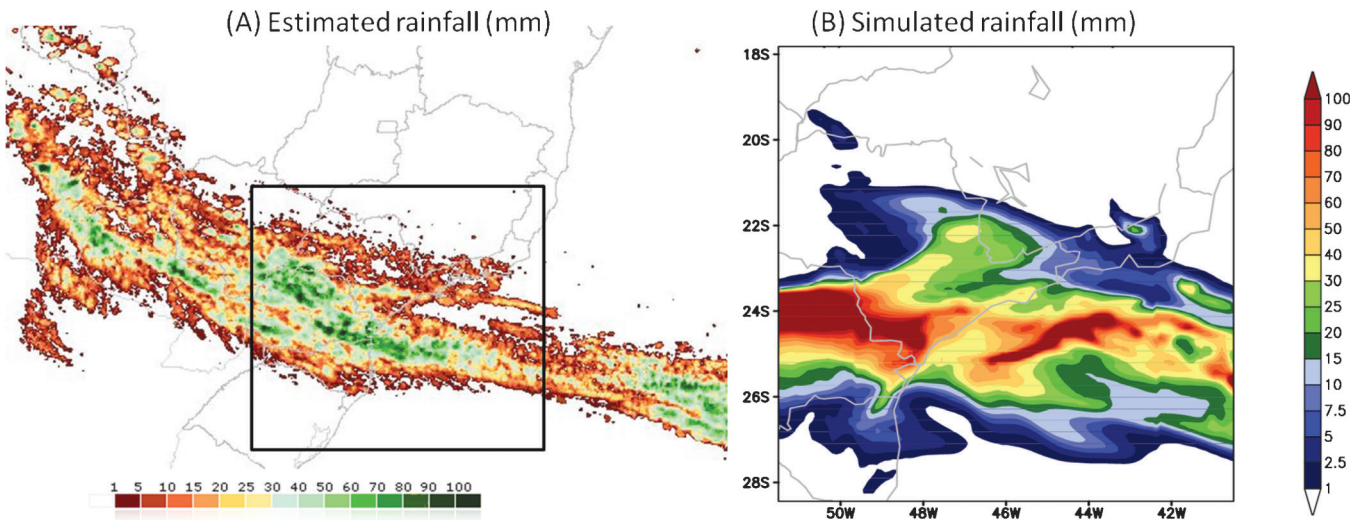


**Figure 11.** (a) 24-hour accumulated rainfall (mm) estimated by remote sensing for 18 August 2008. (b) Same but simulated by model. Note that the color bars of the two legends are not equivalent.

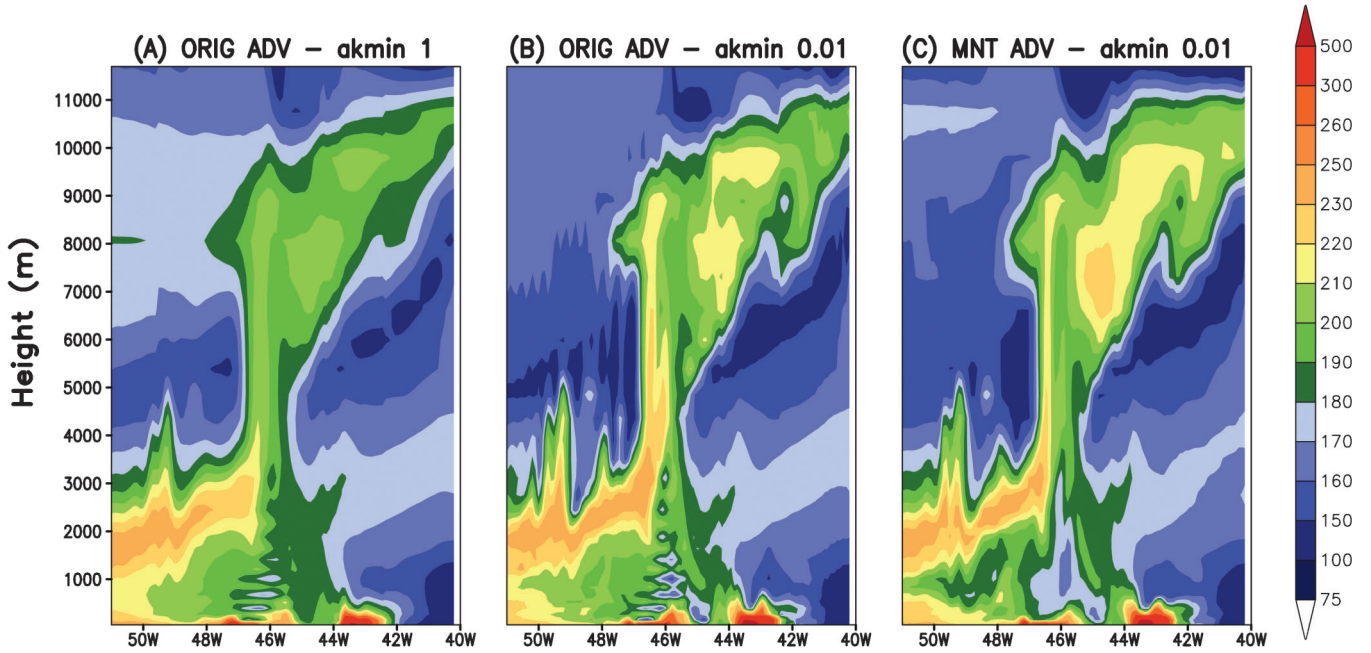


**Figure 12.** Vertical tracer transport by a deep convective system. (a) Results from the orig scheme and strong diffusion. (b) Same, but with weaker diffusion. (c) Results from the mnt scheme and weaker diffusion.

46 W. Increasing the diffusion ( $akmin = 1$ , Figure 12a), the spurious oscillations are reduced but the tracer distribution is also smoother. Reductions of up to 15% in the mass mixing ratio in the convective core and detrainment zone are noted. On the other hand, the mnt advection even with weak diffusion ( $akmin = 0.01$ ) does not generate spurious oscillations (Figure 12c) and seems to produce much more realistic transport and tracer distribution patterns.

The horizontal transport at upper levels of tracer mass detrained by shallow convective systems is shown in Figure 13. This figure shows the tracer mixing ratio at a height of 5.4 km, where the prevailing horizontal wind flows from the west with a speed of around 20 m/s. Several tracer cores detrained by convective systems are also shown. Figures 13a and 13b show the tracer distributions resulting from the orig advection scheme and  $akmin$  equal to 1 and 0.01, respectively. As shown in Figure 13b, the orig advection with a weak diffusion again produces spurious oscillations (denoted by the white arrows) with under- and overshoots. Increasing the diffusion (Figure 13a), the spurious oscillations are almost eliminated, but the tracer distribution is much smoother. In particular, the two cores contoured by the black circle in Figure 13b are not evident in Figure 13a. The simulation presented in Figure 13b also has the lowest and highest values of the tracer mixing ratio, an indication of a non-monotonic scheme. Figure 13c shows the tracer distribution using the mnt scheme and weak diffusion. As before, spurious oscillations did not appear and the convective tracer cores are well defined, without under- and overshoots.

#### 4. Impact on Transport of Emissions Associated With Sharply Localized Sources and on Formation of Secondary Chemical Species

Sources associated with biomass burning are important examples of sharply localized emission fields, which produce plumes with strong spatial gradients of pollutant concentration. To study the impact of both advection schemes on transport and chemical formation, we solve the mass continuity equation, which in its advective form, after Reynolds decomposition and neglecting molecular diffusion, reads [e.g., Seinfeld and Pandis, 1998]

$$\frac{\partial \bar{\eta}_k}{\partial t} + \underbrace{\bar{u}_i \frac{\partial \bar{\eta}_k}{\partial x_i}}_I + \underbrace{\frac{1}{\bar{\rho}_a} \frac{\partial (\bar{\rho}_a \overline{\eta_k'' u_i''})}{\partial x_i}}_{II} = \underbrace{\bar{Q}_k}_{III}, \quad (24)$$

where  $\bar{\eta}_k$  is the grid box average of the mass mixing ratio of species  $k$ , term (I) represents the 3-D resolved transport (advection by the mean wind which is denoted by  $\bar{u}_i$ ), term (II) is the sub-grid scale transport by the unresolved flows ( $\overline{\eta_k'' u_i''}$  are the sub-grid scale fluxes) and term (III) is the forcing. The quantity  $\bar{\rho}_a$  is the grid box average of the dry air density. The forcing  $\bar{Q}_k$  is split into sink ( $R$ ), source ( $E$ ) and the net production or loss by additional physical and/or chemical processes ( $PL$ )

$$\bar{Q}_k = R + E + PL. \quad (25)$$

In this study, the biomass burning sources were prepared using the trace gas and aerosol emission fields preprocessor described by Freitas et al. [2011]. The biomass burning

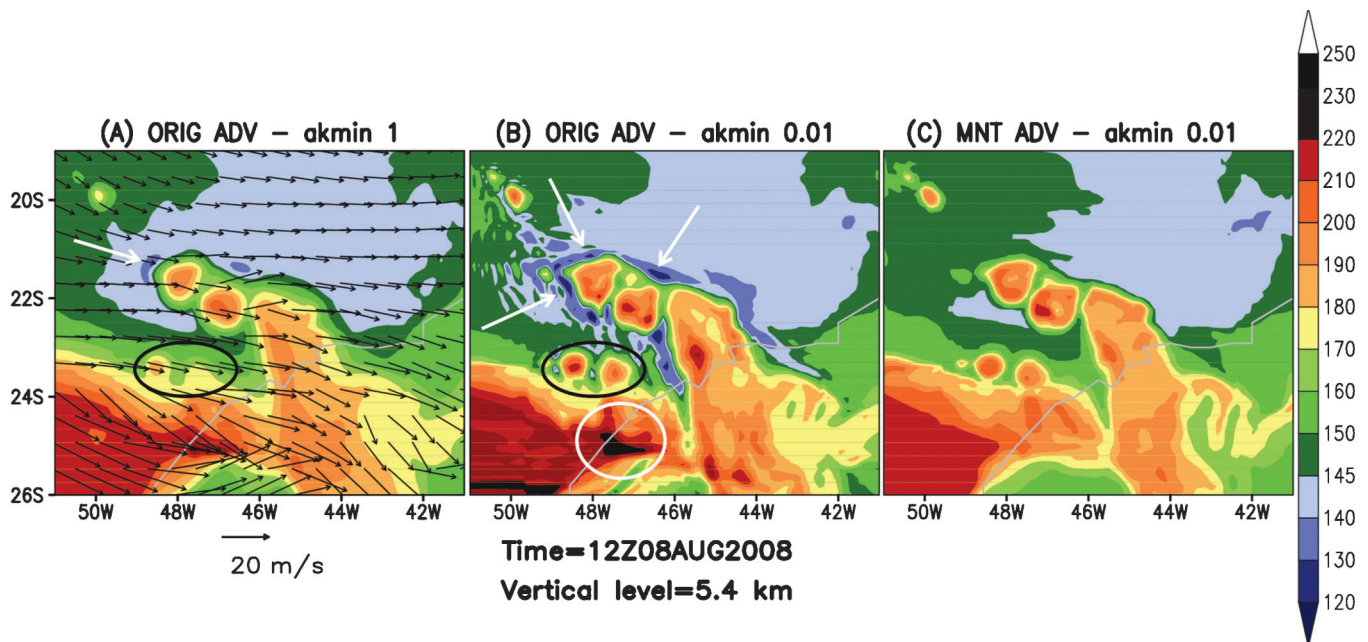


**Figure 13.** Horizontal transport of detrained mass tracer by convective systems. (a) The tracer mass mixing ratio using the orig advection and stronger diffusion. Also, the prevailing horizontal wind is shown. (b) Same, but with weaker diffusion. (c) Same as Figure 13b but using the mnt advection scheme.

emission estimate [Longo *et al.*, 2010] is split into two contributions: smoldering, which releases material in the first model layer above the surface, and flaming, which makes use of an in-line 1-D plume rise model to determine the injection layer [Freitas *et al.*, 2007, 2010]. The net production or loss ( $PL$ ) by chemical reactivity is calculated using the RACM chemical mechanism [Stockwell *et al.*, 1997], and more details are provided by Longo *et al.* (submitted manuscript, 2011).

Model runs were done to assess the impact of the advection schemes. The model was configured with the same grid of the previous section (see Figure 14). The soil model is composed of 7 layers with variable resolution, distributed within the first 5 meters of soil depth. The total length of the time integration was 2 days, starting on 16 June 2008 at 00 UTC. As before, atmospheric and chemical initial and boundary conditions were provided by the 6 hourly CPTec T126L28 analysis and MOCAGE simulation fields, respectively. Initial soil moisture was taken from Gevaerd and Freitas' [2006] estimation technique. The soil temperature was initialized assuming a vertically homogenous field defined by the air temperature closest to the surface from the atmospheric initial data. Figure 14 also shows the fire locations, as retrieved by remote sensing on the 2nd day of the simulation, as well as the carbon monoxide emission strength. A huge fire was observed close to the geographical coordinate (48 W, 22 S), denoted by the red arrow. We use this particular fire to analyze the impact of the advection schemes on the transport and chemical reactivity of its emissions.

Figure 15 shows the simulation of the transport of the smoke plume associated with the big fire from Figure 14 at 22:30 UTC on 17 June 2008. Four simulations were done, where three used the orig advection scheme (with  $akmin = 1, 0.1$  and  $0.01$ ) and one used the mnt scheme (with  $akmin = 0.01$ ). As described before, the fire emissions are split into two parts. The smoldering part is released at the surface and it appears in the left side of Figure 15 as smoke (actually carbon monoxide - CO) distributed between the surface and the first 1 km of height and around longitude 48 W. The flaming emission is injected in the upper levels by the 1-D plume rise model and appears in the same figure as the downwind plume located between 3 and 5.6 km of height. Note that at this time the horizontal size of this plume is around 200 km. From Figure 15a, the orig scheme with stronger diffusion simulates a much smoother and wider CO mass distribution, not only for the elevated plume but as well as just above the surface. In this simulation, the maximum value of CO mixing ratio inside the elevated plume is around 400 ppbv. As expected, reducing the diffusion (Figures 15b–15d) results in more defined plumes, stronger gradients and higher maximum values. The maximum values of CO mixing ratio inside the elevated plumes are 800 and 1100 ppbv for the simulations with the orig scheme and  $akmin$  equal to 0.1 and 0.01, respectively. Note also the undershoots with values below than 50 ppbv present in the last simulation (denoted by the white areas in Figure 15c). In case of the mnt scheme with  $akmin$  equal to 0.01 (Figure 15d), the maximum value is 850 ppbv. Associated with the differences in the spatial gradient of

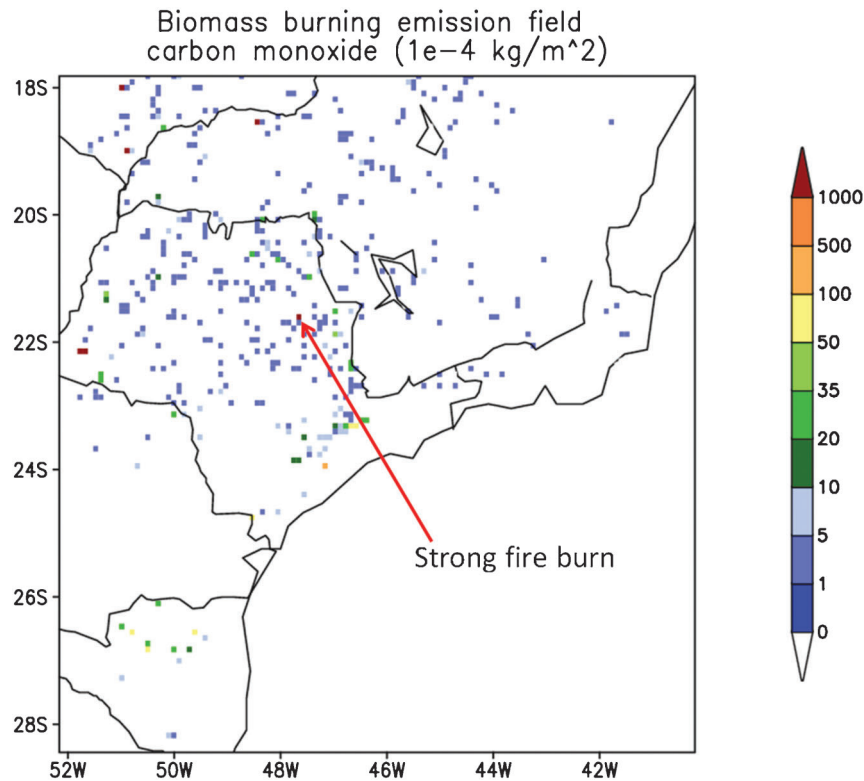


**Figure 14.** Model simulation domain, fire locations and associated carbon monoxide emission field ( $10^{-4} \text{ kg m}^{-2}$ ). Also, the strong fire burn used in this study is shown.

the tracers produced by both advection schemes and the applied diffusion, significant discrepancies in the mass concentration of secondary chemical species are expected, mainly the ones for which its net production or loss are determined by non-linear relationships. The right side of Figure 15 reflects this expectation. It shows the ozone ( $\text{O}_3$ ) mixing ratio distribution from the surface up to a height of 5.9 km. The results for  $\text{O}_3$  mixing ratio inside the smoke plume at this nocturnal time (19:30 LT) show a dipole pattern with a depletion of  $\text{O}_3$  at the source region and an excess downwind. The  $\text{O}_3$  depletion is caused by its consumption by nitric oxide (NO) produced by the combustion of the biomass and injected inside the plume (not shown), while the downwind ozone excess is associated with the horizontal transport of the air mass rich in ozone formed in the early hours and during the daytime.

Figures 15e–15g correspond to results for  $\text{O}_3$  with the orig scheme and  $\text{akmin}$  equal to 1, 0.1 and 0.01, respectively. For the case using the orig scheme and stronger diffusion (Figure 15e), the dipole pattern is not evident, reflecting the strong mixing present in the simulation. The two other simulations with the same advection, but weaker diffusion (Figures 15f and 15g), have similar patterns and mixing ratios between themselves. Differences in the  $\text{O}_3$  mixing ratio of up to +50% in the region with depleted ozone and up to –20% downwind can be found in the previous three simulations. Figure 15h introduces the

results for the  $\text{mnt}$  scheme. In the elevated plume, it simulates values for  $\text{O}_3$  of around 10% more than the orig scheme with the same level of diffusion. Also, when compared with the simulation with stronger diffusion, the differences are much larger.

A horizontal view of the CO plume as simulated by both advection schemes and different strengths of diffusion is depicted in Figure 16. The results refer to a height of 3.9 km and at the same time previously discussed. The horizontal distribution of CO simulated by the orig scheme with different intensities of diffusion (Figures 16a–16c) presents huge discrepancies. The stronger diffusion (Figure 16a) produces a wide and smooth distribution but seems to prevent spurious oscillations. In the plume core, the maximum value of the CO mixing ratio is about 400 ppbv. Decreasing the diffusion (Figures 16b and 16c) results in horizontally narrow plumes with higher gradients and maximum values (1400 and 900 ppbv, respectively) of the CO mixing ratio. However, spurious oscillations appear, with large under- and overshoots. For example, undershoots of less than 10 ppbv in a background of around 50–75 ppbv are generated. On the other hand, the  $\text{mnt}$  advection, even with weak diffusion, does not generate spurious oscillations (Figure 16d) and seems to produce much more realistic horizontal transport and tracer distribution patterns. The plume is much more narrow and the maximum value present in its core is about 1200 ppbv.

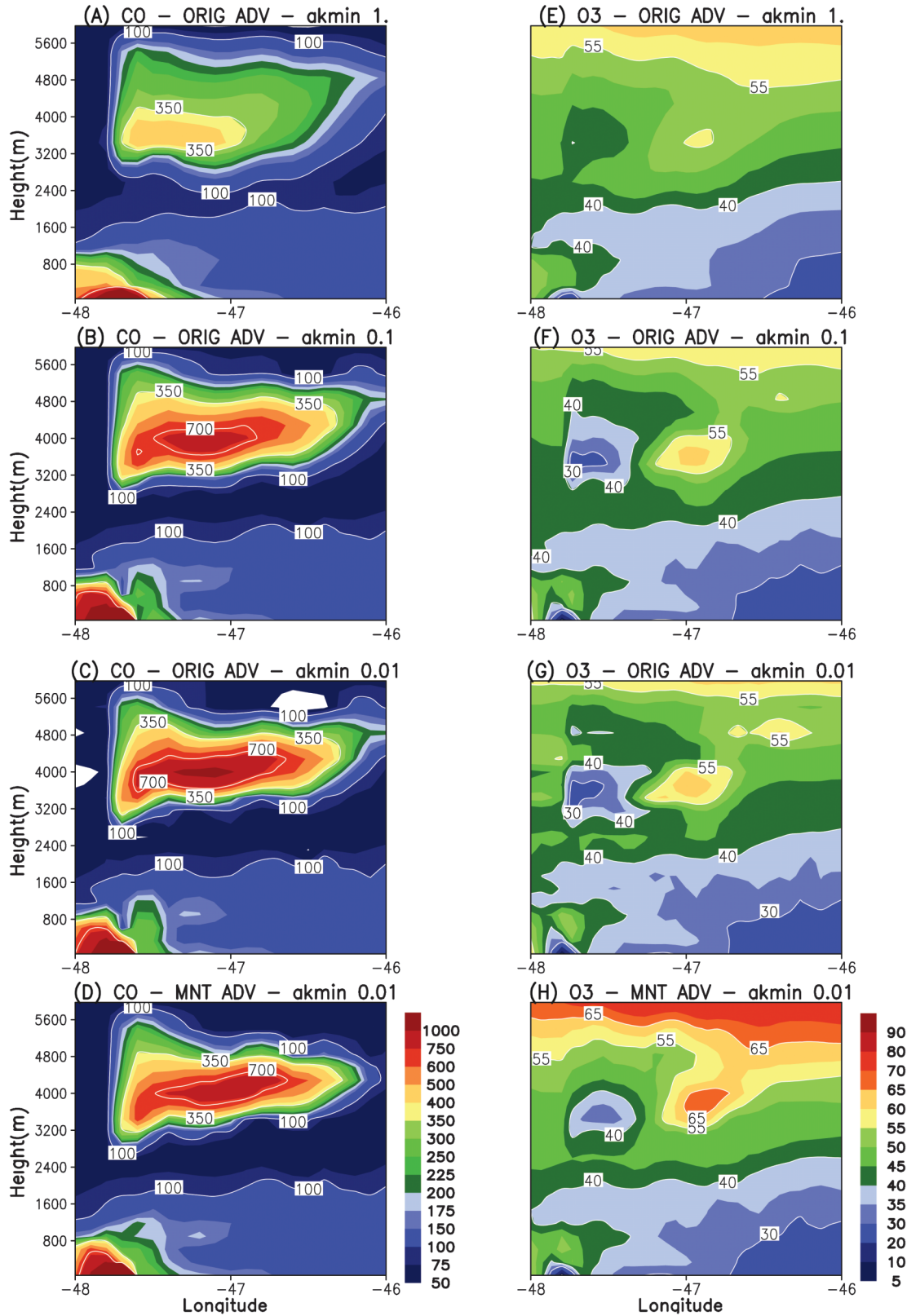


**Figure 15.** Four simulations of a smoke plume at 22:30 UTC on 17 June 2008 produced by the fire denoted by the red arrow in Figure 14. (a–d) The carbon monoxide (CO) mass mixing ratio (ppbv) as simulated with the orig advection scheme and akmin equal to 1, 0.1, and 0.01 in Figures 15a, 15b, 15c, respectively. Figure 15d shows the same tracer but simulated with the mnt advection and akmin = 0.01. (e–h) The same simulations but for ozone (O<sub>3</sub>).

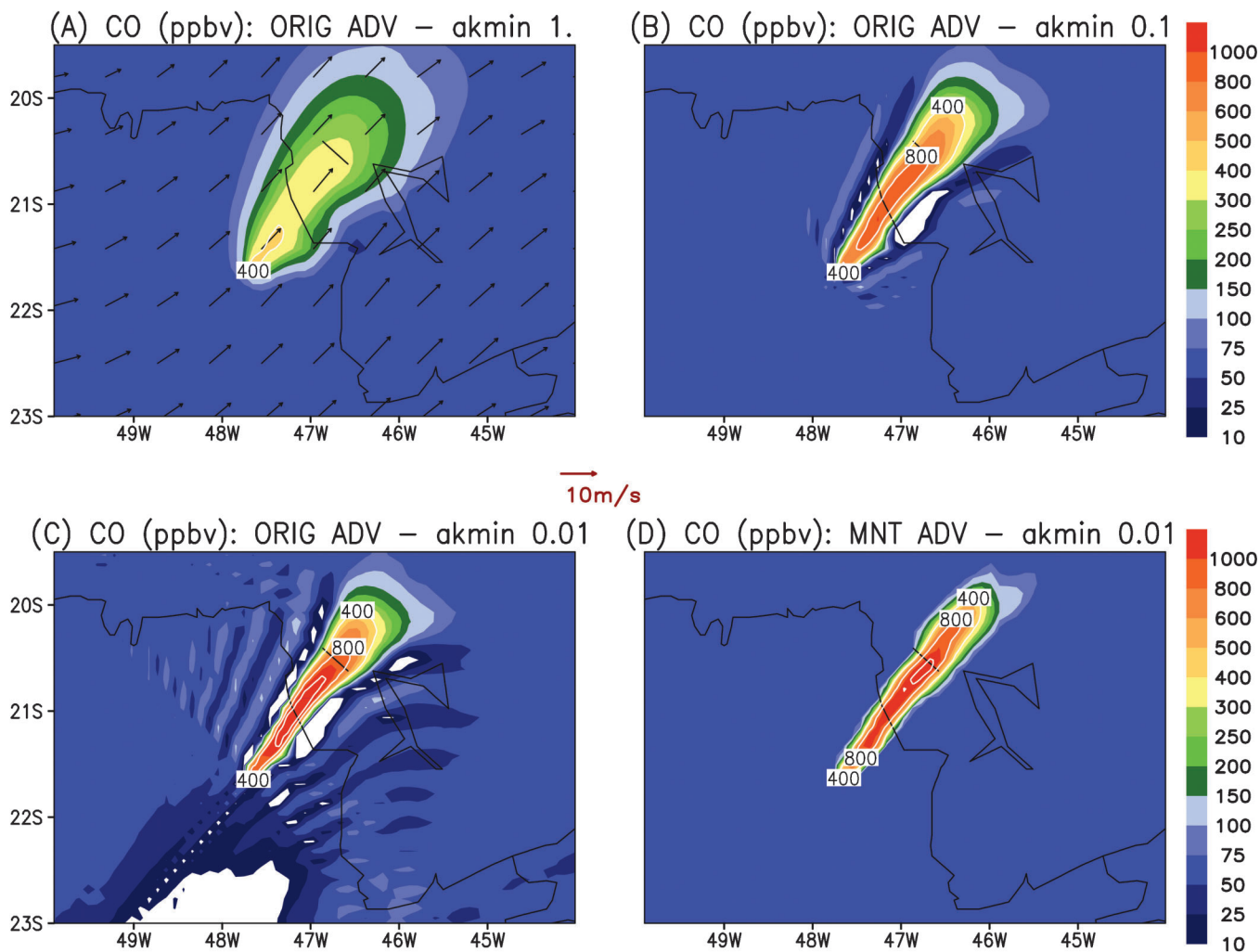


**Figure 16.** Four simulations of the carbon monoxide (ppbv) plume produced by the fire denoted by the red arrow in Figure 14. The results correspond to the time 22:30 UTC on 17 June 2008 and at a height of 3.9 km. The results with the orig advection scheme and akmin equal to (a) 1, (b) 0.1, and (c) 0.01, respectively. (d) The same tracer but simulated with the mnt advection and akmin = 0.01.

Figure 17 introduces a horizontal view at a height of 3.5 km of the ozone mass mixing ratio (ppbv) distribution as simulated by both schemes. The dipole pattern is again evident, more or less depending on the level of diffusion used. Up to 50% more ozone is present in the downwind region for the simulations with weaker diffusion. The simulation with the orig scheme and akmin 0.01 (Figure 17c) seems to be unrealistic, with strong and spurious oscillations. The mnt one (Figure 17d) produces more realistic patterns and well defined plume boundaries in terms of ozone.

## 5. Discussion and Conclusions

An additional advection transport scheme was implemented in the CCATT-BRAMS regional atmospheric chemistry transport model and its performance in transporting sharply localized tracer fields from biomass burning was compared against the original formulation. The main properties of the new scheme are: (1) its ability to maintain the initial

monotonic characteristics of a tracer field being advected and (2) its relatively low intrinsic numerical diffusion.

Several tests using idealized 2-D non-divergent and divergent, stationary and time-dependent wind fields as well as 3-D realistic wind flows with data assimilation and full model atmospheric physics were performed. The results showed that the new scheme produces much more realistic transport patterns, without generating spurious oscillations, under- or overshoots, or spreading mass away from the local peaks. On the other hand, with the original advection scheme, which is not monotonic, spurious oscillations, under- and overshoots are normally present in the simulations.

A remedy to remove the spurious oscillations and maintain the monotonicity of the field in the original advection scheme is by increasing the numerical diffusion through the horizontal diffusion parameterization. However, this process causes an excessive smoothing in the tracer distribution, reducing the local gradients, maximum

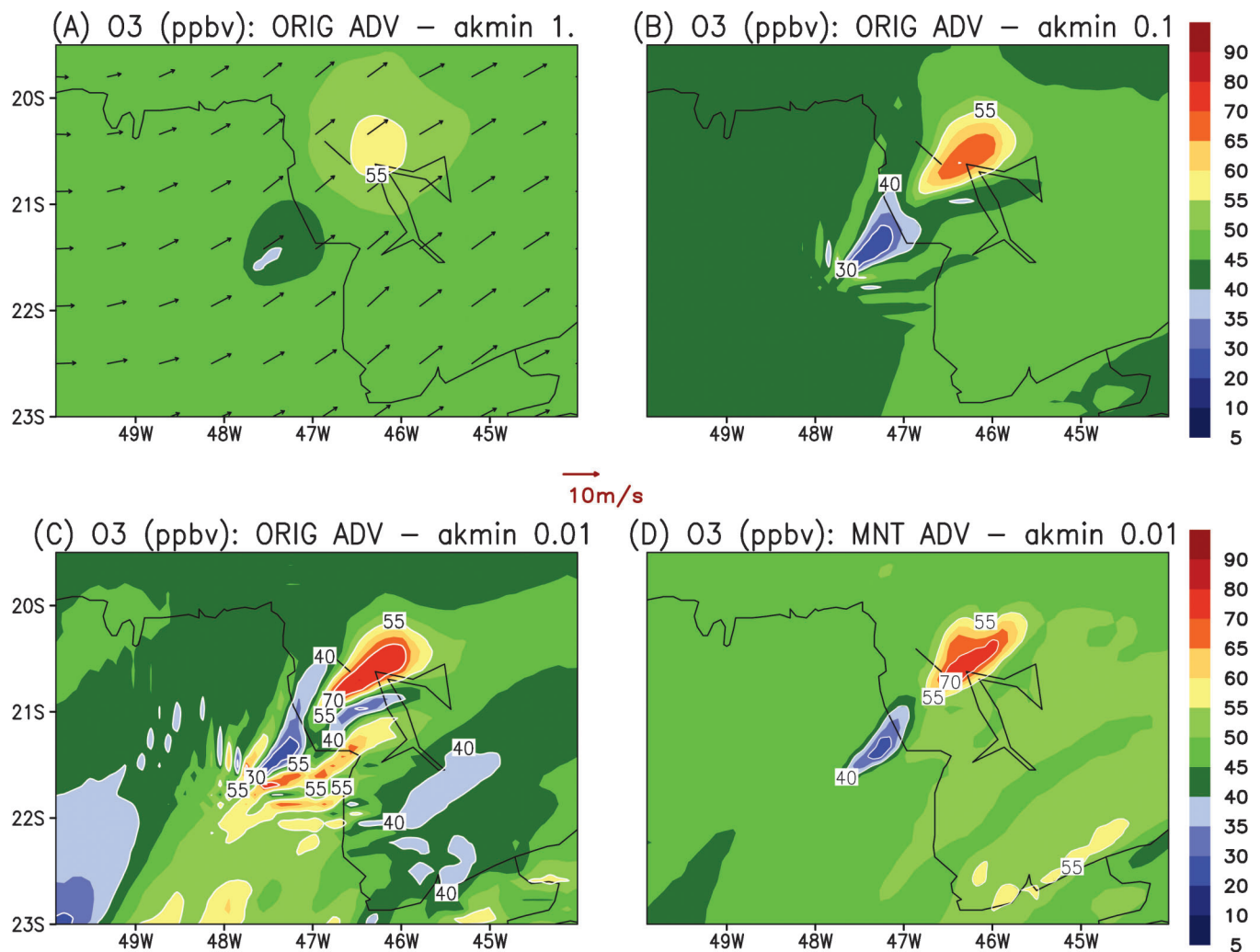


**Figure 17.** Four simulations of the ozone (ppbv) plume produced by precursors from the fire denoted by the red arrow in Figure 14. The results correspond to the time 22:30 UTC on 17 June 2008 and at a height of 3.5 km. The results with the orig advection scheme and akmin equal to (a) 1, (b) 0.1, and (c) 0.01, respectively. (d) The same tracer but simulated with the mnt advection and akmin = 0.01.

values and unrealistically spreading mass away from the local peaks produced by strongly localized sources. The excessive smoothing in the precursors of secondary species (like ozone) formed by non-linear chemical reactions causes large differences in the calculated mixing ratio. In our example, described in Section 4, differences of up to 50% were seen for ozone inside the smoke plume core.

In spite of the huge improvements shown with the mnt scheme, we should note that this scheme also exhibits some unphysical anti-diffusion (Figure 6). Disadvantages of the mnt scheme are also related to its computational aspects. The case study presented in Section 4 required about 30% more computer time for the run with the mnt scheme than that with the orig advection. Furthermore, looking for monotonicity imposes a two pass sweep on the input data (upstream and downstream) in distinct orders (ascending and descending). Data dependencies prevent parallelism in the sweeping direction, imposing severe restrictions on

domain decomposition. However, the extra computer resource needed by the mnt scheme is fairly justified by the vast improvements in the simulation.

Overall, the mnt scheme provides much better numerical representation of the advective transport and will replace the orig scheme of the CCATT-BRAMS modeling system. Future work will focus on improving the listed shortcomings of the mnt scheme. Further comparisons with state-of-the-art/highly accurate advection algorithms like CSLAM [Lauritzen *et al.*, 2010] will also be pursued.

#### Appendix A: Initial Condition for the Tracers of the Idealized Experiments

1. The tracer fields used in Sect. 3.1.2 are defined by the following equations using arbitrary units for the mass mixing ratio (where  $X = x/10$  km and  $Y = y/10$  km are the grid box indexes, in the range [1,100]):

Square:

$$Tr = \begin{cases} 100, & \left\{ \begin{array}{l} \text{if } (40 \leq X \leq 60, 05 \leq Y \leq 25) \\ \text{if } (40 \leq X \leq 60, 75 \leq Y \leq 95) \end{array} \right. \\ 20, & \text{otherwise} \end{cases} \quad (\text{A1})$$

Slot:  $Tr = Tr_A + Tr_B$ , where

$$Tr_A = \begin{cases} 100, & \left\{ \begin{array}{l} \text{if } \sqrt{(X-50)^2 + (Y-25)^2} \leq 15 \\ \text{if } \sqrt{(X-50)^2 + (Y-75)^2} \leq 15 \end{array} \right. \\ 20, & \text{otherwise} \end{cases} \quad (\text{A2a})$$

$$Tr_B = \begin{cases} -80, & \left\{ \begin{array}{l} \text{if } (48 \leq X \leq 65, 23 \leq Y \leq 27) \\ \text{if } (35 \leq X \leq 52, 73 \leq Y \leq 77) \end{array} \right. \\ 0, & \text{otherwise} \end{cases} \quad (\text{A2b})$$

Triangular:  $Tr = Tr_A + Tr_B + 20$ , where

$$\left\{ \begin{array}{l} Tr_A = 80 \left( \max \left( 0, 1 - \frac{1}{15} \sqrt{(X-50)^2 + (Y-25)^2} \right) \right) \\ Tr_B = 80 \left( \max \left( 0, 1 - \frac{1}{15} \sqrt{(X-50)^2 + (Y-75)^2} \right) \right) \end{array} \right. \quad (\text{A3a})$$

$$\left( \right) \quad (\text{A3b})$$

Gaussian:

$$Tr = \min \left( 20, 100 \left( \exp \left( -\frac{(X-50)^2 + (Y-25)^2}{150} \right) + \exp \left( -\frac{(X-50)^2 + (Y-75)^2}{150} \right) \right) \right) \quad (\text{A4})$$

2. The Gaussian tracer field used in Sect. 3.1.3 is given by

$$Tr = 20 + 80 \left( \exp \left( -\frac{(X-25)^2 + (Y-50)^2}{250} \right) + \exp \left( -\frac{(X-75)^2 + (Y-50)^2}{250} \right) \right) \quad (\text{A5})$$

where  $X = x/10$  km and  $Y = y/10$  km are the grid box indexes, in the range [1,100].

3. The first test, discussed in Sect. 3.1.5, employed three tracers whose initial conditions were defined by:

$$\left\{ \begin{array}{l} Tr_1 = \min \left( 20, 100 \exp \left( -\frac{(X-50)^2 + (Y-25)^2}{150} \right) \right) \\ Tr_2 = \min \left( 30, 145 \exp \left( -\frac{(X-60)^2 + (Y-28)^2}{300} \right) \right) \\ Tr_3 = 360 - Tr - Tr_2 \end{array} \right. \quad (\text{A6})$$

where  $X$  and  $Y$  are the grid box indexes, in the range [1,100].

The second test employed four tracers, where the first two are the same as shown in equation (A6), while the other two are defined as:

$$\left\{ \begin{array}{l} Tr_3 = 40 + \frac{3Tr_1 + 6Tr_2}{4} \\ Tr_4 = Tr_1 + Tr_2 + Tr_3. \end{array} \right. \quad (\text{A7})$$

## Appendix B: The RAMS Horizontal Diffusion

In RAMS, when the horizontal grid spacing is large, the horizontal diffusion parameterization (based on the K-theory) uses a horizontal eddy mixing coefficient given by Smagorinsky [1963]

$$K_{horiz} = (c_x \Delta x)^2 \sqrt{2 \left( \frac{\partial \bar{u}}{\partial x} \right)^2 + 2 \left( \frac{\partial \bar{v}}{\partial y} \right)^2 + \left( \frac{\partial \bar{u}}{\partial x} + \frac{\partial \bar{v}}{\partial y} \right)^2}, \quad (\text{B1})$$

where  $c_x$  is a constant,  $\Delta x$  is the horizontal grid spacing and  $\bar{u}$  and  $\bar{v}$  are the horizontal components of the grid scale wind field. However, the actual horizontal eddy mixing coefficient used obeys the following relationship

$$K_{horiz}^{effec} = \max [K_{horiz}^{\min}, K_{horiz}], \quad (\text{B2})$$

where  $K_{horiz}^{\min}$  is a imposed minimum value given by

$$K_{horiz}^{\min} = 0.075 akmin (\Delta x)^{4/3}. \quad (\text{B3})$$

In equation (B3)  $akmin$  is a user-specified coefficient of order 1. Equation (B2) is justified to prevent very small horizontal diffusion coefficients in situations when the local fluid deformation rate happens to be close to zero, resulting in very weak diffusion and too noisy simulations. More details can be found at <http://www.atmet.com/html/docs/documentation.shtml>.

**Acknowledgments.** We acknowledge partial support of this work by CNPq (302696/2008-3, 309922/2007-0). The authors would like to thank the anonymous reviewers and the editor for the careful review of our manuscript and providing us with their comments and suggestions to improve its quality.

## References

- Crowley, W. P. (1968), Numerical advection experiments, *Mon. Weather Rev.*, 96, 1–11, doi: [10.1175/1520-0493\(1968\)096<0001:NAE>2.0.CO;2](https://doi.org/10.1175/1520-0493(1968)096<0001:NAE>2.0.CO;2).
- Freitas, S. R., K. M. Longo, M. Silva Dias, P. Silva Dias, R. Chatfield, E. Prins, P. Artaxo, G. Grell, and F. Recuero (2005), Monitoring the transport of biomass burning emissions in South America, *Environ. Fluid Mech.*, 5(1–2), 135–167, doi: [10.1007/s10652-005-0243-7](https://doi.org/10.1007/s10652-005-0243-7).
- Freitas, S. R., K. M. Longo, R. Chatfield, D. Latham, M. A. F. Silva Dias, M. O. Andreae, E. Prins, J. C. Santos, R. Gielow, and J. A. Carvalho Jr (2007), Including the sub-grid scale plume rise of vegetation fires in low resolution atmospheric transport models, *Atmos. Chem. Phys.*, 7, 3385–3398, doi: [10.5194/acp-7-3385-2007](https://doi.org/10.5194/acp-7-3385-2007).
- Freitas, S. R., et al., (2009), The Coupled Aerosol and Tracer Transport model to the Brazilian developments on the Regional Atmospheric Modeling System (CATT-BRAMS)—Part 1: Model description and evaluation, *Atmos. Chem. Phys.*, 9, 2843–2861, doi: [10.5194/acp-9-2843-2009](https://doi.org/10.5194/acp-9-2843-2009).
- Freitas, S. R., K. Longo, J. Trentmann, and D. Latham (2010), Technical Note: Sensitivity of 1D smoke plume rise models to the inclusion of environmental wind drag, *Atmos. Chem. Phys.*, 10, 585–594, doi: [10.5194/acp-10-585-2010](https://doi.org/10.5194/acp-10-585-2010).
- Freitas, S. R., K. M. Longo, M. F. Alonso, M. Pirre, V. Marecal, G. Grell, R. Stockler, R. F. Mello, and M. Sánchez Gácita (2011), PREP-CHEM-SRC – 1.0: A preprocessor of trace gas and aerosol emission fields for regional and global atmospheric chemistry models, *Geosci. Model Dev.*, 4, 419–433, doi: [10.5194/gmd-4-419-2011](https://doi.org/10.5194/gmd-4-419-2011).
- Gevaerd, R., and S. R. Freitas (2006), Estimativa operacional da umidade do solo para iniciação de modelos de previsão numérica da atmosfera. Parte I: Descrição da metodologia e validação, *Rev. Bras. Meteorol.*, 21(3), 1–15.
- Hundsdoerfer, W., and J. G. Verwer (2007), *Numerical Solution of Time-Dependent Advection-Diffusion-Reaction Equations*, Springer Ser. Comput. Math., vol. 33, 471 pp., Springer, Berlin.
- Lanser, D., and J. G. Verwer (1998), Analysis of operator splitting for advection-diffusion-reaction problems from air pollution modeling, Rep. MAS-R9805, CWI, Amsterdam.
- Lauritzen, P. H., R. D. Nair, and P. A. Ullrich (2010), A conservative semi-Lagrangian multi-tracer transport scheme (CSLAM) on the cubed-sphere grid, *J. Comput. Phys.*, 229, 1401–1424, doi: [10.1016/j.jcp.2009.10.036](https://doi.org/10.1016/j.jcp.2009.10.036).
- Lauritzen, P. H., P. A. Ullrich, and R. D. Nair (2011), Atmospheric transport schemes: Desirable properties and a semi-Lagrangian view on finite-volume discretizations, in *Numerical Techniques for Global Atmospheric Models*, Lect. Notes Comput. Sci. Eng., vol. 80, edited by P. H. Lauritzen et al., 185–250, Springer, Berlin.
- LeVeque, R. J. (1996), High-resolution conservative algorithms for advection in incompressible flow, *SIAM J. Numer. Anal.*, 33(2), 627–665, doi: [10.1137/0733033](https://doi.org/10.1137/0733033).
- Lin, S.-J., and R. B. Rood (1996), Multidimensional flux-form semi-Lagrangian transport schemes, *Mon. Weather Rev.*, 124, 2046–2070, doi: [10.1175/1520-0493\(1996\)124<2046:MFFSLT>2.0.CO;2](https://doi.org/10.1175/1520-0493(1996)124<2046:MFFSLT>2.0.CO;2).
- Longo, K. M., S. R. Freitas, M. O. Andreae, A. Setzer, E. Prins, and P. Artaxo (2010), The Coupled Aerosol and Tracer Transport model to the Brazilian developments on the Regional Atmospheric Modeling System (CATT-BRAMS)—Part 2: Model sensitivity to the biomass burning inventories, *Atmos. Chem. Phys.*, 10, 5785–5795, doi: [10.5194/acp-10-5785-2010](https://doi.org/10.5194/acp-10-5785-2010).
- McRae, G. J., W. R. Goodin, and J. H. Seinfeld (1982), Numerical solution of the atmospheric diffusion equation for chemically reacting flows, *J. Comput. Phys.*, 45(1), 1–42, doi: [10.1016/0021-9991\(82\)90101-2](https://doi.org/10.1016/0021-9991(82)90101-2).
- Medvigy, D., P. Moorcroft, R. Avissar, and R. Walko (2005), Mass conservation and atmospheric dynamics in the Regional Atmospheric Modeling System (RAMS), *Environ. Fluid Mech.*, 5(1–2), 109–134, doi: [10.1007/s10652-005-5275-5](https://doi.org/10.1007/s10652-005-5275-5).
- Nair, R. D., and P. H. Lauritzen (2010), A class of deformational flow test cases for linear transport problems on the sphere, *J. Comput. Phys.*, 229(23), 8868–8887, doi: [10.1016/j.jcp.2010.08.014](https://doi.org/10.1016/j.jcp.2010.08.014).
- Ovtchinnikov, M., and R. C. Easter (2009), Nonlinear advection algorithms applied to interrelated tracers: Errors and implications for modeling aerosol–cloud interactions, *Mon. Weather Rev.*, 137, 632–644, doi: [10.1175/2008MWR2626.1](https://doi.org/10.1175/2008MWR2626.1).
- Peuch V.-H., M. Amodei, T. Barthet, M.-L. Cathala, B. Josse, M. Michou, and P. Simon (1999), MOCAGE, MODèle de Chimie Atmosphérique à Grande Echelle, in *Proceedings of Météo-France Workshop on Atmospheric Modelling*, pp. 33–36, Météo-France, Toulouse, France.
- Plumb, R. A. (2007), Tracer interrelationships in the stratosphere, *Rev. Geophys.*, 45, RG4005, doi: [10.1029/2005RG000179](https://doi.org/10.1029/2005RG000179).
- Plumb, R., and M. Ko (1992), Interrelationships between mixing ratios of long-lived stratospheric constituents, *J. Geophys. Res.*, 97(D9), 10,145–10,156, doi: [10.1029/92JD00450](https://doi.org/10.1029/92JD00450).
- Prather, M. J. (1986), Numerical advection by conservation of second-order moments, *J. Geophys. Res.*, 91(D6), 6671–6681, doi: [10.1029/JD091iD06p06671](https://doi.org/10.1029/JD091iD06p06671).
- Rood, R. B. (1987), Numerical advection algorithms and their role in atmospheric transport and chemistry models, *Rev. Geophys.*, 25, 71–100, doi: [10.1029/RG025i001p00071](https://doi.org/10.1029/RG025i001p00071).
- Seinfeld, J., and S. Pandis (1998), *Atmospheric Chemistry and Physics*, John Wiley, New York.

- Skamarock, W. C., and M. L. Weisman (2009), The impact of positive-definite moisture transport on NWP precipitation forecasts, *Mon. Weather Rev.*, *137*, 488–494, doi: [10.1175/2008MWR2583.1](https://doi.org/10.1175/2008MWR2583.1).
- Smagorinsky, J. (1963), General circulation experiments with the primitive equations. Part I. The basic experiment, *Mon. Weather Rev.*, *91*, 99–164, doi: [10.1175/1520-0493\(1963\)091<0099:GCEWTP>2.3.CO;2](https://doi.org/10.1175/1520-0493(1963)091<0099:GCEWTP>2.3.CO;2).
- Stockwell, W. R., F. Kirchner, M. Kuhn, and S. Seefeld (1997), A new mechanism for regional atmospheric chemistry modeling, *J. Geophys. Res.*, *102*(D22), 25,847–25,879, doi: [10.1029/97JD00849](https://doi.org/10.1029/97JD00849).
- Thuburn, J., and M. E. McIntyre (1997), Numerical advection schemes, cross-isentropic random walks, and correlations between chemical species, *J. Geophys. Res.*, *102*(D6), 6775–6797, doi: [10.1029/96JD03514](https://doi.org/10.1029/96JD03514).
- Tremback, C., J. Powell, W. Cotton, and R. Pielke (1987), The forward in time upstream advection scheme: Extension to higher orders, *Mon. Weather Rev.*, *115*, 540–555, doi: [10.1175/1520-0493\(1987\)115<0540:TFTUAS>2.0.CO;2](https://doi.org/10.1175/1520-0493(1987)115<0540:TFTUAS>2.0.CO;2).
- Van Leer, B. (1977), Toward the ultimate conservative difference scheme, IV: A new approach to numerical convection, *J. Comput. Phys.*, *23*(3), 276–299, doi: [10.1016/0021-9991\(77\)90095-X](https://doi.org/10.1016/0021-9991(77)90095-X).
- Walcek, C. J. (2000), Minor flux adjustment near mixing ratio extremes for simplified yet highly accurate monotonic calculation of tracer advection, *J. Geophys. Res.*, *105*(D7), 9335–9348, doi: [10.1029/1999JD901142](https://doi.org/10.1029/1999JD901142).
- Walko, R., *et al.*, (2000), Coupled atmosphere-biophysics-hydrology models for environmental modeling, *J. Appl. Meteorol.*, *39*(6), 931–944, doi: [10.1175/1520-0450\(2000\)039<0931:CABHMF>2.0.CO;2](https://doi.org/10.1175/1520-0450(2000)039<0931:CABHMF>2.0.CO;2).
- Wang, H., W. C. Skamarock, and G. Feingold (2009), Evaluation of scalar advection schemes in the advanced research WRF model using large-eddy simulations of aerosol–cloud interactions, *Mon. Weather Rev.*, *137*, 2547–2558, doi: [10.1175/2009MWR2820.1](https://doi.org/10.1175/2009MWR2820.1).
- Williamson, D. L., J. B. Drake, J. J. Hack, R. Jakob, and P. N. Swarztrauber (1992), A standard test set for numerical approximations to the shallow water equations in spherical geometry, *J. Comput. Phys.*, *102*(1), 211–224, doi: [10.1016/S0021-9991\(05\)80016-6](https://doi.org/10.1016/S0021-9991(05)80016-6).
- Yanenko, N. A. (1971), *The Method of Fractional Steps*, 160 pp., Springer, Berlin.